



## Supplementary Materials for

### **Performing Mathematical Operations with Metamaterials**

Alexandre Silva, Francesco Monticone, Giuseppe Castaldi, Vincenzo Galdi, Andrea Alù,  
Nader Engheta\*

\*Corresponding author. E-mail: [engheta@ee.upenn.edu](mailto:engheta@ee.upenn.edu)

Published 10 January 2014, *Science* **343**, 160 (2014)  
DOI: 10.1126/science.1242818

#### **This PDF file includes:**

Materials and Methods

Supplementary Text

Figs. S1 to S23

Tables S1 and S2

References

## Materials and Methods

### Graded Refractive Index (GRIN)

The RF module in frequency domain from the full-wave commercial software simulator COMSOL Multiphysics™, version 4.3a, is used for all simulations presented in the main text and for the GRIN structures mentioned in this Supplementary Material (SM). The schematic model used in the simulations for the metasurface (MS) approach with the 2 two-dimensional (2D) GRIN sub-blocks and a MS or a meta-transmit-array (MTA) positioned between them is shown in Fig. S1. The wavelength chosen for all presented examples is  $\lambda_0 = 3\mu\text{m}$  (details are given in the meta-transmit-array design subsection); however, the same basic system can be applied, in principle, to any wavelength of interest, depending only on the material parameters and the dimensions according to the desired characteristic distance  $L_g$ . The whole system (GRIN/MS/GRIN or GRIN/MTA/GRIN) presented here is limited by the width  $W$  in the transverse direction  $y$ , and by the total length  $d1 + L_g + \Delta + L_g + d2 + d3 = 3L_g$  in the longitudinal direction  $x$  as can be seen in Fig. S1. This total length is chosen to be larger than the length of the basic system  $2L_g + \Delta$ . Outside the GRIN, the material is defined as air, and each side air region has a width of  $W/2$ . The external boundaries are defined as “scattering boundary condition”. Extra perfectly-matched-layer (PML) regions with thickness  $d4 = \lambda_0 / 4$  are used on top and bottom of the model for additional absorption of the leaking fields. A distance of  $d1 = 10.5\mu\text{m}$  is used to merely keep a separation between the position where the input function is applied and the external boundary on the left. This is done to monitor possible reflections from this boundary.

In the GRIN design step, one has to define  $W$  and  $L_g$ , so the material for the GRIN can be designed following  $\varepsilon(y) = \varepsilon_c \left\{ 1 - \left[ \pi / (2L_g) \right]^2 y^2 \right\}$ , where  $\varepsilon_c$  is the permittivity at the central plane of the 2D GRIN and  $L_g$  is the characteristic length, and  $\mu = \mu_0$ . If realistic materials are to be used, one can have  $\varepsilon_c$  defined and use the same formula to find  $W$  and/or  $L_g$ .

The MS and MTA thicknesses can be  $\Delta \ll \lambda_0$ . Some MS examples we successfully simulated are as small as  $\lambda_0 / 60$  (not shown here). However, the length used for the MS examples presented in the main text is  $\Delta = \lambda_0 / 3 = 1\mu\text{m}$ , chosen to be the same length as the designed MTA in order to have fair comparisons between both cases. Details for the MTA design are shown later in this SM. The characteristic distance is chosen to be  $L_g = 35\mu\text{m}$  (approximately  $12\lambda_0$ ). The GRIN material is designed using the following parameters:  $W = 10\lambda_0 = 30\mu\text{m}$ ,  $L_g = 35\mu\text{m}$ ,  $\varepsilon(\pm W/2) = 1.1\varepsilon_0$ , which result in  $\varepsilon_c \approx 2.01\varepsilon_0$ . However, the exact value used for  $W$  in the examples is  $W = 29.75\mu\text{m}$  (approximately  $10\lambda_0$ ) in order to be, again, the same as the designed MTA, since it is easier to adapt the MS and the GRIN dimensions and materials in the simulations than to redesign the whole MTA for a different GRIN width.

In our models (Fig. S1), the domains on the right of the MS,  $L_g + d2$ , can be filled with GRIN(+) or GRIN(-), where both materials are described in the main text. In the case of GRIN(-), the extra distance  $d2 = 16.5 \mu\text{m}$  from the position  $L_g$ , where output fields are observed, is necessary in order to avoid the “noise” due to excitation of surface plasmon polaritons (SPPs) at the boundary between GRIN(+) and GRIN(-). The last domain of length  $d3 = 7 \mu\text{m}$  is added to separate the GRIN(-) from the external PML, since this latter works better when in contact with a positive-permittivity material. The choice of the exact values of  $d1$ ,  $d2$ ,  $d3$ , and the air regions given above is not crucial, as they just need to be large enough to yield clear results.

Meshing can be a challenging process in such model because the mesh size may be a sensitive parameter. Sometimes, if the mesh from 0 to  $+W/2$  in the transversal direction is very different from the mesh from 0 to  $-W/2$ , even if it is highly refined, simulation results can be adversely affected. To avoid this, a central line is used to allow us to copy and mirror the mesh from the upper part to the lower part of the GRIN. The maximum mesh cells settings used here are:  $\lambda_0/12$  (250nm) for GRIN (+ and -) with a maximum element growth rate of 1.1,  $\lambda_0/60$  (50nm) for the MS,  $\lambda_0/200$  (15nm) for the MTA, and a maximum element growth rate of 1.01 in air.

Although Fig. S1 is the complete model used, results presented in the main text and in this SM show only the area of interest comprised by  $(L_g + \Delta + L_g) \times W$ . For all GRIN models, the electric field vector is oriented along the  $z$  axis.

### Metasurface design

We know from the literature that an arbitrary linear convolution operation between a (input) function  $f(y)$  and a Green’s function  $G(y)$ , associated with a desired operator of choice, can generate an (output) function  $g(y) = \int f(u) G(y-u) du$ . This operation can be represented, in the Fourier space, as  $\tilde{g}(k_y) = \tilde{G}(k_y) \tilde{f}(k_y)$ , where the tilde indicates Fourier transform. It is also well known that a GRIN waveguide performs one Fourier transform at each characteristic distance  $L_g$  (24), which means that, by the simple wave propagation along the GRIN, we can have the function  $\tilde{f}(k_y)$  where, in this case, the Fourier variable  $k_y$  is in the same domain of  $y$ , so  $y$  plays the role of  $k_y$ . Now, our goal is to obtain  $\tilde{G}(y)$ , that is our transfer function, only by the propagation of the wave signal through a medium of length  $\Delta$ , allowing us to have the desired output function  $g(y)$  after the wave propagates another  $L_g$ . This can be accomplished by properly designed filters, in our case, MSs. It is worth remembering that the GRIN with realistic materials can perform a Fourier transform but not an inverse Fourier transform. So, in a real case, we will be exploring the relation  $\mathcal{F}\{\mathcal{F}[g(y)]\} \propto g(-y)$ , with  $\mathcal{F}(\cdot)$

denoting Fourier transform, which implies that the output will be proportional to a mirror image of the desired output function  $g(y)$ .

The first MS to be designed is for differentiation. In this case, we base our design in the Fourier transform property that relates the  $n^{th}$  derivative of a function to its first Fourier transform,  $d^n f(y)/dy^n = \mathcal{F}^{-1}\{(ik_y)^n \mathcal{F}[f(y)]\}$ , from where the function  $(ik_y)^n$ , or  $(iy)^n$  as explained before, will be used as our transfer function  $\tilde{G}(y) \propto (iy)^n$ . Therefore, our MS has to change the amplitude and phase of the field profile that has already propagated for a distance  $L_g$  along the GRIN and, at this point is proportional to the first Fourier transform of the input function, in a way that, after the field has propagated along its length  $\Delta$ , the output field profile should resemble the function  $(iy)^n \mathcal{F}[f(y)]$ . As we are avoiding gain media and the GRIN lateral dimension is finite and limited by  $W$ , we have to normalize the transfer function to the lateral limit of GRIN, ensuring that the transmission coefficient stays below unity throughout the transverse plane, so the desired transfer function becomes  $\tilde{G}(y) \propto [iy/y_0]^n$ , where  $y_0 = W/2$ . It means that the MS alters the amplitude and phase of the impinging wave by  $e^{ik\Delta} = [iy/(W/2)]^n$ ; where  $k = k_0 \sqrt{[\varepsilon_{ms}(y)/\varepsilon_0][\mu_{ms}(y)/\mu_0]}$ , with  $k_0 = 2\pi/\lambda_o$ ,  $\varepsilon_{ms}(y)$  and  $\mu_{ms}(y)$  being the permittivity and permeability of the metasurface at point  $y$ , respectively,  $\lambda_o$  being the free-space wavelength of operation, and  $\Delta$  the thickness of the metasurface.

Assuming that the GRIN is approximately impedance matched to free space for waves paraxially impinging on it, we can use  $\varepsilon_{ms}(y)/\varepsilon_0 = \mu_{ms}(y)/\mu_0$  to reduce reflections from the MS. This leads to:  
 $k = k_0 \sqrt{[\varepsilon_{ms}(y)/\varepsilon_0][\mu_{ms}(y)/\mu_0]} = k_0 \sqrt{\varepsilon_{ms}^2(y)/\varepsilon_0^2} = k_0 \varepsilon_{ms}(y)/\varepsilon_0$ . Doing this, we have:

$$e^{ik\Delta} = e^{ik_0 \varepsilon_{ms} \Delta / \varepsilon_0} = \left( i \frac{y}{W/2} \right)^n,$$

from which we have

$$\varepsilon_{ms}(y) = \varepsilon_{ms}'(y) + i\varepsilon_{ms}''(y) = \frac{in\varepsilon_0}{k_0\Delta} \ln \left[ -i \frac{W}{2y} \right],$$

with  $\varepsilon_{ms}'(y)$  and  $\varepsilon_{ms}''(y)$  being the real and imaginary parts of  $\varepsilon_{ms}(y)$ . So, the material properties of our differentiator MS are:

$$\varepsilon(y) = \varepsilon_{ms}(y)/\varepsilon_o = \mu_{ms}(y)/\mu_o = i \left[ n\lambda_o / (2\pi\Delta) \right] \ln(-iW/(2y)),$$

In this way, in order to have an output profile proportional to the first derivative (n=1) of the input function,  $g(y) \propto df(y)/dy$ , the volumetric permittivity and permeability functions of the MS are:

$$\varepsilon(y) = \varepsilon_{ms}(y) / \varepsilon_o = \mu_{ms}(y) / \mu_o = i \left[ \lambda_o / (2\pi\Delta) \right] \ln(-iW / (2y)).$$

The results of our numerical simulation (z-component of the electric field for the transverse electric (TE) wave in the system, i.e., with only z-component of the electric field) of the computational metamaterial having  $W = 29.75 \mu m \cong 10\lambda_o$ ,  $L_g = 35 \mu m \cong 12\lambda_o$ ,  $\varepsilon_c = 2.01\varepsilon_o$  and  $\mu = \mu_o$  for the first GRIN(+) sub-block, this first derivative MS ( $\Delta = 1 \mu m = \lambda_o / 3$ ), and a subsequent GRIN(-) sub-block ( $\varepsilon_c = -2.01\varepsilon_o$  and  $\mu = -\mu_o$ ) are shown in Fig. 2B. The input function  $f(y) = aye^{-y^2/b}$ , with  $a = 0.7 \mu m^{-1} = 2.1\lambda_o^{-1}$  and  $b = 10 \mu m^2 = \lambda_o^2 / 0.9$ , is depicted in perspective on the left side of the panel. We also show the snapshot of the field distribution as the wave propagates through the entire system. At the output plane ( $2L_g + \Delta$ ), we obtain the electric field distribution  $g(y)$  shown also in Fig. 2C [after a  $\phi = 8^\circ$  phase adjustment (details in the phase adjustment sub section later in this SM)]. From this figure one can see that the output is indeed proportional to the 1<sup>st</sup> spatial derivative of the input function.

For the second derivative MS (n=2), the transfer function is  $\tilde{G}(y) \propto (iy)^2$  and the volumetric permittivity and permeability functions are:

$$\varepsilon(y) = \varepsilon_{ms}(y) / \varepsilon_o = \mu_{ms}(y) / \mu_o = i \left[ 2\lambda_o / (2\pi\Delta) \right] \ln(-iW / (2y)).$$

Inserting this MS in the same computational metamaterial with the same input function as before, we show the field distribution along the system in Fig. S2A and we compare the output result with the analytical result in Fig. 2E.

Other MSs are designed in the same way, just changing the transfer function to the proper desired operator. In the case of an integration operator, the transfer function is  $\tilde{G}(y) \propto (iy/d)^{-1}$ , where  $d$  is an arbitrary normalizing length, assumed to be  $1 \mu m$  in our example. In order to avoid gain requirements for transmission coefficients with magnitude larger than unity for  $|y| < d$ , we truncate the required transfer function at  $|y| = d$ , and assume its magnitude to be unity for all points within this range. Therefore, the volumetric permittivity and permeability functions for this MS are:

$$\begin{aligned} \varepsilon_{ms}(y) / \varepsilon_o = \mu_{ms}(y) / \mu_o &= i \left[ \lambda_o / (2\pi\Delta) \right] \ln(iy / d) \text{ for } |y| > d, \text{ and} \\ \varepsilon_{ms}(y) / \varepsilon_o = \mu_{ms}(y) / \mu_o &= - \left[ \lambda_o / (4\Delta) \right] \text{sign}(y / d) \text{ for } |y| < d. \end{aligned}$$

Again, inserting this MS surface in the previous computational metamaterial, we can show the field distribution along the system in Fig. S2B and the comparison with the ideal result in Fig. 2F, from where one can notice a good agreement between the curves.

The last MS designed here is for the convolution operator. We design a MS that performs the convolution operation with a rectangular kernel of width  $W_k = 16 \mu m = 5.33 \lambda_o$ . The transfer function corresponding to the Fourier transform of the kernel is  $\tilde{G}(y) \propto \text{sinc}[W_k y / (2s^2)]$ , where  $s = \sqrt{\lambda_o L_g / (\pi^2 \sqrt{\epsilon_c / \epsilon_o})}$  is a GRIN scale factor defined in (24). For such transfer function, the required permittivity and permeability functions are:

$$\epsilon_{ms}(y) / \epsilon_o = \mu_{ms}(y) / \mu_o = i \left[ \lambda_o / (2\pi\Delta) \right] \ln \left[ 1 / \text{sinc}(W_k y / (2s^2)) \right].$$

Results for this MS in the GRIN system are shown in Fig. S2C and Fig. 2G, where the obtained output and the analytical result are in good agreement.

#### “Merging” GRIN with metasurface

We “merge” the MS functionality with the GRIN(+) and GRIN(-), in order to explore the possibility of realizing a single metamaterial block that achieves both Fourier transforming and filtering at the same time. Specifically, instead of three distinct sub-blocks with total length  $2L_g + \Delta$  for the 1<sup>st</sup> differentiation, as shown in Fig. 2A, we investigate the possibility of having only two sections, where section 1 (left half on left panel of Fig. S3) is a block with material parameters obtained after merging (via a simple mixing formula) the permittivity and permeability of the GRIN(+) with half of MS for the 1<sup>st</sup> differentiation, resulting in a metamaterial block with thickness  $L_g + \Delta / 2$ , whose relative permittivity and permeability functions are:

$$\begin{aligned} \epsilon_{\text{merg1}}(y) &= \epsilon(y) / \epsilon_o + i \left[ \lambda_o / (4\pi L) \right] \ln(-iW / (2y)) \text{ and} \\ \mu_{\text{merg1}}(y) &= 1 + i \left[ \lambda_o / (4\pi L) \right] \ln(-iW / (2y)); \end{aligned}$$

section 2 (right half on left panel of Fig. S3) is another block with thickness  $L_g + \Delta / 2$  with material parameters resulted from merging the GRIN(-) with the other half of MS of the 1<sup>st</sup> differentiation:

$$\begin{aligned} \epsilon_{\text{merg2}}(y) &= -\epsilon(y) / \epsilon_o + i \left[ \lambda_o / (4\pi L) \right] \ln(-iW / (2y)) \text{ and} \\ \mu_{\text{merg2}}(y) &= -1 + i \left[ \lambda_o / (4\pi L) \right] \ln(-iW / (2y)). \end{aligned}$$

The output function of our numerical simulation (right panel in Fig. S3) still resembles quite reasonably the expected output (input function is the same  $f(y) = aye^{-y^2/b}$  as before).

### Meta-transmit-array (MTA) design

The MS approach for wave-based computing and signal processing described in the main text requires a control of the wave transmission and low reflections. An independent control of transmission magnitude and phase of waves, particularly at optical frequencies, over small distances poses severe challenges, especially when the reflection needs to be minimized at the same time. Existing designs based on a single infinitesimally thin MS (11)-(12) are largely suboptimal since simple symmetry considerations require half of the energy interacting with the MS to be reflected. Moreover, the transmission phase cannot cover the entire  $[0, 2\pi]$  range for the same polarization of the incident wave, and the orthogonal polarization needs to be used to this aim. Further details and physical insight on such limitations can be found in (27)-(31) and Supplementary Material therein. To overcome these limitations, in (27) the idea of a MTA was introduced, borrowing some relevant concepts from radio-frequency transmit-arrays and frequency selective surfaces. A subwavelength symmetric stack of three MSs, locally modeled as shunt reactances between transmission line segments, was shown to provide the necessary and sufficient degrees of freedom to fully control the transmission phase with ideally 100% efficiency and minimized reflection. The required reactance profiles to realize the desired phase patterns can be readily synthesized at optical frequencies exploiting the optical nanocircuit paradigm introduced in (32)-(33), using "off-the shelf" dielectric and plasmonic materials properly alternated on a subwavelength scale.

The flexibility, simplicity and relative ease of fabrication make the MTA concept the ideal solution to tailor the wave transmission for computing and signal processing applications with real materials. In the proposed MS approach, the structure sandwiched between the GRIN Fourier transform sub-blocks (Fig. 2A) applies the  $\tilde{G}(y)$  operation in the Fourier domain, as explained in the main text. Since, in general, both magnitude and phase variations are implied in  $\tilde{G}(y)$ , the MTA concept introduced in (27) needs to be extended to realize a full control of the transmission magnitude in addition to the phase, while still minimizing the reflection from the structure. This can be achieved by introducing properly tailored losses in the structure, following a generalized design procedure inspired by (27). First, consider the transmission-line model in Fig. S4A, which locally describes a stack of three MSs, where we introduced a parallel resistance in the outer MSs to model Ohmic losses. By solving this transmission line model, we obtain the general conditions on the surface impedances to implement any desired transmission function  $\tilde{G}(y)$  while, at the same time, minimizing reflections. Intuitively, when the desired transmission magnitude is lower than unity, the lossy MTA has to absorb a portion of the impinging energy in order to avoid unwanted reflections.

As an example, in the main text we have used the MTA to implement the 1<sup>st</sup> spatial differentiation. In this case, the normalized transfer function to be implemented is  $\tilde{G}(y) = iy/y_0$ , where  $y_0 = W/2$ . The desired magnitude and phase of  $\tilde{G}(y)$  are shown in Figs Fig. S4B and C, respectively. By solving the transmission line model for this transfer function and enforcing zero reflection, we find the following analytical conditions on the reactances and resistances:

$$\begin{aligned} X_1(y) = X_3(y) &= -Z_d \frac{1 + (y/y_0)^2}{2(y/y_0) + [1 + (y/y_0)^2] \cot(k_d d)}, \\ R_1(y) = R_3(y) &= Z_d \frac{1 + (y/y_0)^2}{1 - (y/y_0)^2}, \text{ and} \\ X_2(y) &= -Z_d \frac{2(y/y_0) \sin^2(k_d d)}{1 + (y/y_0)^2 + 2(y/y_0) \sin(2k_d d)}, \end{aligned} \quad (\text{S1})$$

where  $k_d$  is the propagation constant of the medium (of thickness  $d$ ) separating the MSs, and  $Z_d$  is the characteristic impedance of the transmission-line segments. As in the lossless case (27), it turns out that the two outer MSs need to be equal, which is a general condition for this type of structures working in transmission. Figures S4D-F show the reactance and resistance profiles along the MTA, calculated with Eqs. (S1), assuming a thin air separation of thickness  $d = \lambda_0/10$  between the MSs. In this case, under normal incidence,  $Z_d$  is equal to the free-space characteristic impedance  $Z_0 = 377 \, \Omega$ . If we realize MSs that implement these functions, the transmission coefficient of the whole structure will be exactly  $\tilde{G}(y) = iy/y_0$ .

Following a similar procedure as in (27), these impedance profiles can be realistically implemented at infrared frequencies by exploiting optical nanocircuit concepts (32)-(33). The basic building block, shown on the left in Fig. S5A, is a cube made of a plasmonic and a dielectric portions, which realizes a parallel inductor-capacitor (L-C) circuit when illuminated by an electric field parallel to the interface between the two materials (dimensions are indicated in the caption of Fig. S5). A wide range of capacitive and inductive impedances can be synthesized by locally modifying the relative filling ratio of the two materials. The plasmonic material chosen here is Aluminum-doped ZnO (AZO), which follows a classic Drude model in the mid-infrared range:  $\varepsilon_p = \varepsilon_\infty - \omega_p^2 / [\omega(\omega + i\gamma)]$ , with  $\varepsilon_\infty = 3.3$ ,  $\omega_p = 2\pi \, 352.2 \, \text{THz}$ , and  $\gamma = 2\pi \, 30.4 \, \text{THz}$  (26). Silicon (Si) is used for the dielectric portion, which has relative permittivity  $\varepsilon_{\text{Si}} = 11.77$  at the operating wavelength of  $3 \, \mu\text{m}$  (34). If this unit cell is repeated to form a one dimension grid of nanorods, a MS is obtained, and a stack of three properly designed MSs realizes the complete MTA, as depicted in Fig. S5A, and in the right inset of Fig. 2A. Here, we considered a center-to-center distance of  $\lambda_0/8$  between the MSs, and the resulting total thickness of the MTA is  $\lambda_0/3$  at a wavelength of  $3 \, \mu\text{m}$ . The



proposed MTA has been designed to operate in the infrared range, which may be of strategic interest for defense applications and remote sensing. Nevertheless, the design can, in principle, be scaled at any frequency, provided that materials with plasmonic properties are available and that the smallest features of the structure can be fabricated with current nanotechnology techniques. At an operating wavelength of  $3\ \mu\text{m}$ , AZO has a negative permittivity comparable (in absolute value) to the positive permittivity of Silicon, which guarantees balance between plasmonic and dielectric portions, leading to better performance.

Given the many non-idealities of this proposed practical implementation compared to the ideal transmission-line model, the design of the MTA has been carried out by numerically analyzing the transmission coefficient, varying the filling ratio of the two materials in the inner and outer MSs, and identifying the geometries that give the desired local response. Here, however, we need to independently modulate the transmission magnitude in addition to the phase. As indicated by our transmission-line analysis, this can be achieved by properly tailoring the Ohmic resistances of the outer MSs along the  $y$  direction. We implemented the resistive elements by artificially introducing losses in the dielectric portion of the unit cells; the amount of losses is parameterized by the loss tangent  $\tan \delta$ , namely, the ratio between the resistive and reactive parts of the effective impedance of the dielectric portion, which may correspond to varying the doping and impurity level in the semiconductors. Another equivalent way to introduce losses could be by adding an absorbing material with controlled thickness between neighboring MSs.

Figures S5B and C show the magnitude and phase, respectively, of the transmission coefficient of a periodic MTA varying the width of the plasmonic portion in the inner ( $w_{in}$ ) and outer ( $w_{out}$ ) MSs, in the case of  $\tan \delta = 0$ . Figure S5D shows the magnitude of the reflection coefficient and the white contour lines in all the panels enclose the regions of low reflection. Each point of these contour plots is calculated by an independent full-wave numerical simulation using CST Microwave Studio<sup>TM</sup>. It is clear from these charts that, by locally changing the geometry, it is indeed possible to implement almost any transmission phase together with minimized reflection (27). Then, if the loss tangent is increased, as shown in the three examples in Fig. S6, the transmission magnitude can also be modulated while retaining low reflection. Using these design charts, we identified several different geometries that cover a wide range of transmission phases and magnitudes. By arranging these geometries along the  $y$  axis of the MTA, the desired transverse magnitude and phase profiles can be obtained, combined with low reflection.

For the present example, we have realized the transfer function for the 1<sup>st</sup> spatial derivative  $\tilde{G}(y) = iy/y_0$ , obtaining impedance profiles qualitatively consistent with the ones predicted by our transmission-line model in Fig. S4. Figure S7A shows the calculated electric field distribution in the case of a linearly-polarized plane wave impinging on the MTA. The transverse profiles of transmission magnitude and phase are in very good agreement with the desired ones, as clearly shown in Fig. S7B. It is also evident that the impinging wave is only marginally reflected from the MTA, and we have

verified that the reflection coefficient remains low over a reasonable bandwidth around the central frequency of 100 THz (Fig. S7C).

The lossy MTA described in this section represents a practical, efficient and flexible solution to realize the desired transfer functions  $\tilde{G}(y)$  in the Fourier domain for our MS approach, and allows fast optical computing and signal processing over a subwavelength thickness. In Figs. Fig. S2D and 2D, one can see the field distribution along our GRIN(+)/MTA/GRIN(+) system and the output results compared to the analytical result for the first derivative of the previous input function, respectively.

### Design of multi-layered slabs for Green's function approach

In the main text, we have proposed the concept of a multi-layered slab capable of realizing the (GF) kernel associated with a linear, space-invariant mathematical operation of choice as a second approach to obtain computational metamaterials. In this case, we avoid the need of going into the Fourier domain, hence avoiding the GRIN sub-blocks that perform the Fourier and inverse Fourier transforms as in our first approach. In order to implement directly the spatial Fourier transform of the kernel  $\tilde{G}(k_y)$ , we need to design a structure that realizes the desired transmission coefficient as a function of the transverse momentum  $k_y$  of the impinging plane wave. In this work, we concentrate on the propagating portion of the spatial spectrum, i.e., propagating plane waves with  $|k_y| < k_0$ . Nevertheless, an extension to the evanescent portion of the spectrum can be envisioned. Even limiting ourselves to the spatial harmonics  $|k_y| < k_0$ , the problem of designing a structure implementing the desired  $\tilde{G}(k_y)$  does not admit a general closed-form analytical solution. In other words, given the desired angular transmission spectrum, it is generally challenging to find the characteristics of the structure that produces such response, and, in general, the inverse problem of synthesizing this response is complicated. As mentioned in the main text, the framework of non-local transformation optics (29) can be used to address this problem for an infinite medium. Here, however, we consider a multi-layered finite slab transversely homogenous, but longitudinally inhomogeneous, composed of  $N$  parallel slabs, as shown in Fig. 3A. The synthesis can be tackled by treating the problem as a nonlinear optimization problem, and solving it numerically. In particular, we minimize the difference between the desired kernel  $\tilde{G}(k_y)$  and the transmission coefficient of the multi-layered slab  $\tilde{T}(k_y)$  within the range  $0 < k_y < k_0$  (in view of the even symmetry), for both real and imaginary parts. The error function is defined as the sum of the squares of the differences at a finite number  $M$  of samples, viz.,

$$err = \sum_{i=1}^M w_r \left( \text{Re} \left[ \tilde{G}(k_{y,i}) - \tilde{T}(k_{y,i}) \right] \right)^2 + w_i \left( \text{Im} \left[ \tilde{G}(k_{y,i}) - \tilde{T}(k_{y,i}) \right] \right)^2, \quad (\text{S2})$$

where  $w_r$  and  $w_i$  are weight coefficients that can be used to selectively penalize the real and imaginary parts, respectively. Throughout this section and in the corresponding part of the main text, we assume an impinging plane wave with transverse magnetic (TM) polarization (i.e.,  $z$ -directed magnetic field). An extension to dual-polarization operation can be readily envisioned, by increasing the number of available degrees of freedom and optimizing for both polarizations.

The commercial software Matlab<sup>TM</sup> offers a number of numerical algorithms to solve unconstrained minimization problems. Since the function to be minimized is not very smooth over the parameter space, we have verified that "simplex algorithms" (e.g., the Nelder-Mead simplex algorithm (35), implemented in Matlab by the function *fminsearch*) work better than multi-dimensional steepest descent or gradient-based methods. Moreover, the strong nonlinear nature of the problem implies a dense concentration of local minima, and hence the solution can be highly dependent on the starting point. Given these considerations, we implemented a fast synthesis algorithm, based on the simplex optimization method, which finds the dielectric permittivity, magnetic permeability and thickness of the  $N$  layers that minimize the error function (S2). The initial point is moved across a reasonable range of parameters in order to search for the minimum in different regions of the multi-dimensional parameter space. Even though there is no guarantee that the proposed approach converges to the global minimum, we found that it usually provides solutions that are sufficiently good for our purpose, i.e., with sufficiently small error-function residual. This synthesis approach allows one to design a multi-layered slab whose transmission coefficient  $\tilde{T}(k_y)$  approximates accurately the desired transfer function  $\tilde{G}(k_y)$  for all the impinging angles within the range  $0 < k_y < k_0$ .

As an example, in the main text we considered the case of the 2<sup>nd</sup> spatial differentiation, whose transformed kernel is  $\tilde{G}(k_y) \propto -k_y^2$ . This is a purely real function that decreases monotonically for increasing transverse momentum. Our synthesis approach is applied to tailor the plane-wave transmission coefficient of a multi-layered slab to match this function. However, since only passive media are considered here, the magnitude of the transmission coefficient has to be always less than unity. Accordingly, we implemented the desired kernel scaled by the constant factor  $k_0^2$ . Given the linearity of the considered operation, the output can be restored by simply amplifying it by this factor. In our optimization algorithm, we considered  $N = M = 10$  samples and layers, and we optimized the permittivity and thickness of each layer, whereas the relative permeability was kept equal to unity in the entire structure. Notice that 10 layers give the sufficient degrees of freedom (two for each layer) to impose both the real and imaginary parts of the transmission coefficient at the 10 sample points. The best results were obtained with weights  $w_r = 2$  and  $w_i = 1$  (i.e., with moderately stronger penalization of the error on the real part) and an initial guess characterized by relative permittivity  $\varepsilon_r = 1$  and thickness  $d = \lambda_0/9$  for all the layers. Figures S8A and B show, respectively, the real and imaginary parts of the optimized transmission spectrum (blue line), compared with

the desired  $\tilde{G}(k_y)$  (red line). A very good agreement is obtained for both real and imaginary parts over almost the entire considered spatial spectrum, except for transverse momenta close to the upper extreme, because the transmission coefficient has to vanish for grazing angles ( $k_y = k_0$ ). Notice that it is not trivial to have a flat imaginary part equal to zero, as even a free space region has a complex transmission coefficient  $\tilde{G}_0(k_y) = \exp\left(i\sqrt{k_0^2 - k_y^2}d\right)$  with non-zero imaginary part function of  $k_y$ . If we perform the inverse Fourier transform of the optimized transfer function in Fig. S8A and B, we obtain the GF of the slab  $G(y)$  shown in Fig. S8C.  $G(y)$  represents the spatial impulse response of the structure, i.e., the output of the slab to the input of a Dirac delta function. The optimized GF is in very good agreement with the desired response shown in Fig. S8D, which is the 2<sup>nd</sup> spatial derivative of the delta function  $G(y) = \delta''(y)$ , low-pass filtered in the region  $|k_y| < k_0$ .

The permittivity and thickness of each layer obtained with our optimization approach are listed in Table S1. The obtained values are reasonable, and the first and third layers are so thin that can be essentially removed, hence reducing the number of layers to eight. The multi-layered slab may be fabricated at optical frequencies by depositing each material in a stack transversely homogenous and layered in the longitudinal direction. For example, at infrared frequencies, the different material permittivities (positive, negative and near zero) can be obtained by tuning the plasma frequency of doped semiconductors, e.g., AZO, changing the doping level of aluminum, which has been suggested for use in our MTA. In principle, a large-area metamaterial slab of this kind may be realized with available nanotechnology techniques. The complete structure is low-profile and thin, as the overall thickness of the computational metamaterial is approximately  $1.2\lambda_0$ .

In the second example shown in the main text, we designed a multi-layered slab that performs the convolution between a generic input function and a rectangular Green's function kernel of width  $\lambda_0$ , i.e.,  $G(y) = \text{rect}(y/\lambda_0)$ . The corresponding transformed kernel in Fourier domain to be implemented is proportional to a sinc function  $\tilde{G}(k_y) \propto \text{sinc}(\pi k_y/k_0)$ , with only the main lobe in the propagating region  $|k_y| < k_0$ , since the first zero occurs exactly at  $k_0$ . Again, we applied the same optimization approach to minimize the difference between the transmission coefficient of the slab and the desired function. Here, we consider a smaller number of samples and layers,  $N = M = 5$ , and the relative permeability is again kept at unity everywhere. The best results are found for a starting point with relative permittivity  $\varepsilon_r = 1$  and thickness  $d = \lambda_0/7$  for all layers, and equal weights  $w_r = w_i = 1$ . The optimized transmission spectrum (blue line) is shown in FigsFig. S9A and B compared with the desired  $\tilde{G}(k_y)$ . As it is evident from these plots, excellent agreement is achieved. Compared with the case of the 2<sup>nd</sup> spatial differentiation in Fig. S8, here the sinc function is more easily implemented since the transmission

coefficient of the structure naturally vanishes at  $k_y = k_0$ . As a result, the Green's function of the slab (Fig. S9C), obtained by inverse-Fourier transforming the optimized transfer function, is also in very good agreement with the desired kernel function  $G(y) = \text{rect}(y/\lambda_0)$ , low-pass filtered in the region  $|k_y| < k_0$  (Fig. S9D). The relative permittivity and thickness of each layer obtained with our optimization approach are listed in Table S2. Once again, these values are reasonable and may be practically implemented. Remarkably, the complete structure is even thinner than the previous example, as the total thickness is only  $0.37\lambda_0$ .

## Supplementary Text

### Phase adjustment issue

An issue that should be addressed is that for a system comprised of GRIN(+) only, like in the MTA case presented in the main text and in the other examples below, sometimes an extra phase factor  $\exp(i\phi)$  has to be applied to the output function. This means that the desired output is obtained not exactly at  $t = 0$ , but at a later time within one period of the field oscillation. This is expected, as explained in [24]. However, this issue is not usually taken into account in the literature because, in typical applications of GRIN structures, one is more interested in the magnitude of the final profile, rather than the phase of the profile acquired through actual wave propagation along the system. Although the amount of phase correction of the output function in the GRIN system can be obtained from the mathematical expression given in [24, due to the inevitable numerical noise in our simulation, this phase can be slightly different from the one obtained using the analytical formula. Therefore, in our case, one needs to determine this phase adjustment from the simulation data to clearly show that the desired field profile is achieved even though not at  $t = 0$ . It is worth noting that, when one uses the combination of GRIN(+) and GRIN(-), such phase adjustment is less crucial [and usually smaller than the case with GRIN(+) and GRIN(+)], since most of the phase accumulated as the wave propagates through the first GRIN(+) would be “undone” and compensated by the propagation through the GRIN(-). A good example of this compensation is the merged MS case where, for all inputs shown here,  $\phi = 0$ . In the all cases presented bellow, unless otherwise specified, the phase adjustment is  $\phi = +7^\circ$ .

### Supporting examples for MS approach

The computational MSs introduced in the main text work even for more complex input functions than the function  $f(y) = ay e^{-y^2/b}$  presented in Fig. 2. Here, we show the results for other input functions applied to the same 10-wavelength-wide GRIN structure with MS [GRIN(+)/MS/GRIN(-)] and with MTA [GRIN(+)/MTA/GRIN(+)].

As a different example of input function for the 1<sup>st</sup> and 2<sup>nd</sup> spatial derivatives, we have chosen the even function  $f(y) = ce^{-y^2/d^2} (4y^2/d^2 - 2)$ , with  $c = 0.5$ , and  $d = \lambda_0/1.5 = 2\mu\text{m}$  depicted in Fig. S10A, which is the second derivative of a Gaussian

function. This same function is also used for the other operators shown in the following. Figure S10B shows a snapshot of the  $z$ -component of the electric field of the wave propagating along the entire metamaterial system, where, in this case, a MS is used between the GRIN(+) and GRIN(-). A point to note in this case is that, as the field propagates along  $x$  and spreads along  $y$ , part of it reaches the edges of the GRIN, getting reflected from and leaking through them. This can cause some “noise” at the output due to the reflected waves from these boundaries. One solution could be to increase  $W$ ; however, as by design we have  $\varepsilon(\pm W/2) = 1.1\varepsilon_0$ , increasing  $W$  would require redesigning the GRIN, i.e., dealing with a whole different system. Another possibility is to increase  $\varepsilon_c$ , but, again, this would be a new system, and comparisons might not be fair. Therefore, keeping the same system, the only way to limit this problem is to scale the input function in a way that its Fourier transform profile fits within  $W$ .

Figures S10C-E present the comparison among the analytical 1<sup>st</sup> spatial derivative of the input function (green line), and the real (red line) and imaginary (blue line) parts obtained at the output of our system ( $2L_g + \Delta$ ), for MS, MTA, and merged MS (MS material merged with GRIN material as explained in the previous section) cases, respectively. Output profiles are multiplied by a constant factor to facilitate comparisons with the analytical profiles. These constant factors are shown explicitly in the figures for each case. Besides, field profile in Fig. S10D has a phase adjustment of  $\phi = -80^\circ$ . One can notice that the output results are in very good agreement with the expected results (for the MTA case, the output profile is mirrored, as explained in the main text).

A more complex input function is the set of quadratic polynomial functions used in Fig. 3B of the main text, but now rescaled to fit within  $W \approx 10\lambda_0$  (Fig. S11A). Figure S11B shows the wave propagation along the GRIN for the MTA case. It is worth recalling that, for the MTA case, the GRIN material after the MTA is GRIN(+). For this input function, part of the field distribution also reaches the edges at  $\pm W/2$ , and one may notice that the second Fourier transform does not occur at distance  $2L_g + \Delta$ , but rather at a position between  $L_g + \Delta$  and  $2L_g + \Delta$ , which can be interpreted as the system having an effective length  $L_{g\_eff}$ . This is due to aberration effects, which are also common in standard lensing systems. Figures S11C and E present the comparison among the analytical 1<sup>st</sup> spatial derivative of the input function, and the real and imaginary parts obtained at the output of our system, for the MS and merged MS cases, respectively. Owing to the aberration effects, Fig. S11D shows the fields observed at  $L_g + \Delta + L_{g\_eff}$  for the MTA case with a phase adjustment of  $\phi = +155^\circ$ . One may notice that even for this complex output, results are in good agreement with the analytical curves.

Another complex input function is the Austin city skyline border (Fig. 3C in the main text). As for the previous case, this function is also scaled down to fit within the width  $W \approx 10\lambda_0$  of the GRIN, as shown in Fig. S12A. Figure S12B shows the wave propagation along the GRIN for the merged MS case, where the boundary between the two regions of merged material can be seen as in Fig. S3. Figures S12C and E present the

comparison among the analytical 1<sup>st</sup> spatial derivative of the input function, and the real and imaginary parts obtained from our simulation at the output of our system, for MS and merged MS cases, respectively. As for the previous function in the MTA case, Fig. S12D shows the fields obtained at  $L_{g\_eff}$  with  $\phi = -55^\circ$  phase adjustment. For both cases, skyline and the set of quadratic polynomial functions,  $L_{g\_eff}$  is the same. One may notice that even for this complex example, where delta functions appear in the results of differentiation, the resulting profiles are in good agreement with the expected results, showing peaks at positions close to the actual delta functions.

As done in the main text, we now show the same three input functions for the metastructure that implements the 2<sup>nd</sup> spatial differentiation operation. Figures S13, S14 and S15 show the results for functions  $f(y) = ce^{-y^2/d^2} (4y^2/d^2 - 2)$ , set of quadratic polynomial functions and skyline, respectively. Again, simulation results are in good agreement with the expected results, showing peaks in positions close to the expected delta functions.

Another set of input functions are presented for the spatial integral operator. They are:  $f(y) = ce^{-y^2/d^2} (4y^2/d^2 - 2)$  (Fig. S16), two inverted rectangular functions with widths of  $1.33\lambda_0 = 4\mu m$  (Fig. S17), and the Gaussian function  $f(y) = e^{-y^2/m^2}$ , with  $m = 5\lambda_0/3 = 5\mu m$  (Fig. S18). The first function shows an excellent agreement with the expected result as can be seen in Fig. S16B. For the case of Fig. S17B, the agreement, with  $\phi = -15^\circ$  phase adjustment, is good in the central part, but deteriorates closer to the edges. This is probably due to the way the MS is defined, since we have avoided the use of gain material in it by truncating the MS design when gain media would be required. However, even using this truncation, the overall result is reasonably good. The last input function (Gaussian) has been chosen to show that, if the desired result does not go to zero at the edges, the result is hindered due to the limited size of the GRIN (Fig. S18B). One can see reflections from the edges of the GRIN in the region between  $L_g + \Delta$  and  $2L_g + \Delta$  in Fig. S18C. If the GRIN was not transversely bounded (i.e., if  $W$  was infinitely large), there would have been no such reflection, bringing the observed electric field closer to the desired function.

The final operator to be presented is the convolution operator. The input functions for this operator are:  $f(y) = ce^{-y^2/d^2} (4y^2/d^2 - 2)$  (Fig. S19), a rectangular function with width of  $5.33\lambda_0 = 16\mu m$  (Fig. S20), and a rectangular function with width of  $2\lambda_0 = 6\mu m$  (Fig. S21). For all cases, the convolution kernel is a rectangular function with width of  $5.33\lambda_0$ . In all examples, the resulting field profiles are in good agreement with the expected analytical responses. It is worth mentioning again that, if the desired function does not go to zero within  $W$ , the final result will be distorted, as it is shown in Fig. S20C. The central part is in good agreement with the analytical result, but when the electric field profile gets closer to the edges of the structure, the result will expectedly

begin to differ from the ideal curve. The phase adjustments are  $\phi = 45^\circ$  in Fig. S19C,  $\phi = -5^\circ$  in Fig. S20C, and  $\phi = 0$  in Fig. S21C.

### Rescaling the GRIN system

The GRIN structure, following the equation  $\varepsilon(y) = \varepsilon_c \left\{ 1 - \left[ \pi / (2L_g) \right]^2 y^2 \right\}$ , is scalable. When we keep the ratio  $W / L_g$  constant, we can have a wider and longer or a narrower and shorter GRIN with the same  $\varepsilon_c$ . Following this approach, we can show what happens at the output of the system GRIN(+)/MS/GRIN(-), with the MS designed to perform the 1<sup>st</sup> spatial differentiation, when the same input function or a scaled input function is used in front of scaled GRIN structures. In the examples shown in Fig. S22, the set of quadratic polynomial functions (Fig. S11A) is the input function for Figs Fig. S22A-C, and the Austin skyline borders (Fig. S12A) is the input function for Figs Fig. S22D-F. In all panels of Fig. S22, red lines are the real part of the output profile obtained at  $2L_g + \Delta$  and green lines are the analytical 1<sup>st</sup> derivative for their respective input functions. Figures S22A and S22D are the output functions when  $W = 10\lambda_0$  and they may be used as the basis for comparisons. If one increases  $W$  to  $30\lambda_0$  ( $L_g$  also becomes three times the original value) and keeps the input function as in the  $10\lambda_0$  case, the output results (Figs Fig. S22B and Fig. S22E, where the dashed lines indicate the  $-5\lambda_0$  to  $5\lambda_0$  region) are quite similar to the original results.

If we also scale the width of the input functions, we may notice some changes on the output profiles, as can be seen in Fig. S22C and Fig. S22F, where the input functions width are also scaled up to  $30\lambda_0$ . In both cases, the input functions encompass three times more wavelengths, and hence more detailed output profiles are obtained. The expected opposite behavior occurs when one scales down the input function. From our simulations, we have found that the minimum  $W$  for which the system GRIN(+)/MS/GRIN(-) for the 1<sup>st</sup> spatial differentiation is still effective for a simple input function, is  $W = 2.5\lambda_0$ .

The total length of our system in this approach needs a certain number of wavelengths, which, depending on the design, can be as large as tens of wavelengths or as small as around six wavelengths. Nonetheless, the overall system size, especially the width, is still several orders of magnitude smaller than conventional lensing systems, thereby allowing wave-based computing and signal-processing over a very small distance. One of the main advantages of this approach is that several different mathematical operators can be designed and easily applied. Even complex input functions can be successfully processed by mathematical operators within a compact system, and the designed structures can be built with realistic materials using available technology.



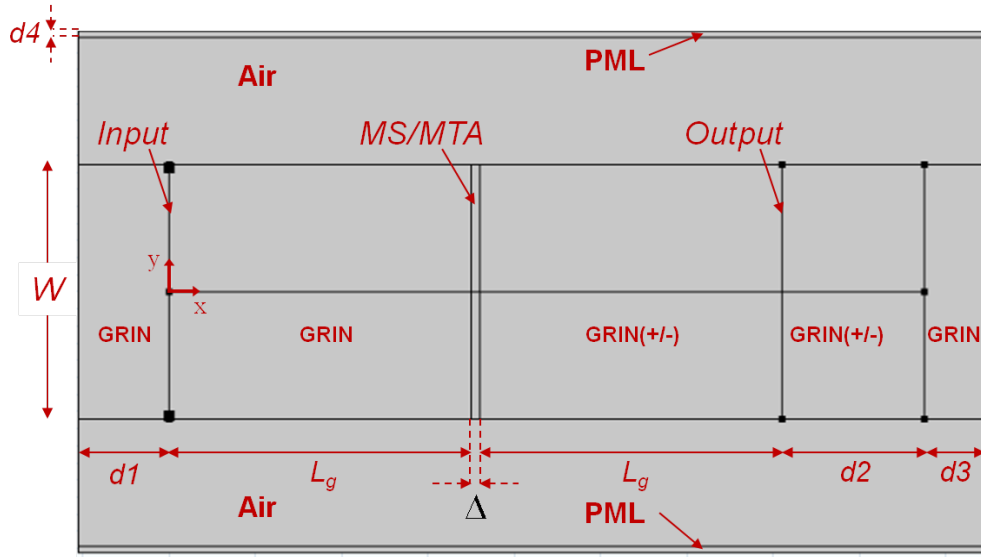
### Supporting examples for GF approach

To further support our concept of computational metamaterials based on directly implementing the GF kernel (GF approach; Fig. 3 of the main text), we show here two additional examples, for the two GF slabs (GFS) discussed in the main text.

Figure S23A shows the 2<sup>nd</sup>-derivative GFS illuminated by the same input function used in Fig. 2,  $f(y) = ay e^{-y^2/b}$ , showing the evolution of the  $z$ -component of the magnetic field distribution [for the transverse-magnetic (TM) wave propagation through the system] within the 10-layered slab. As noticed, the output is indeed closely proportional to the 2<sup>nd</sup> derivative of the input.

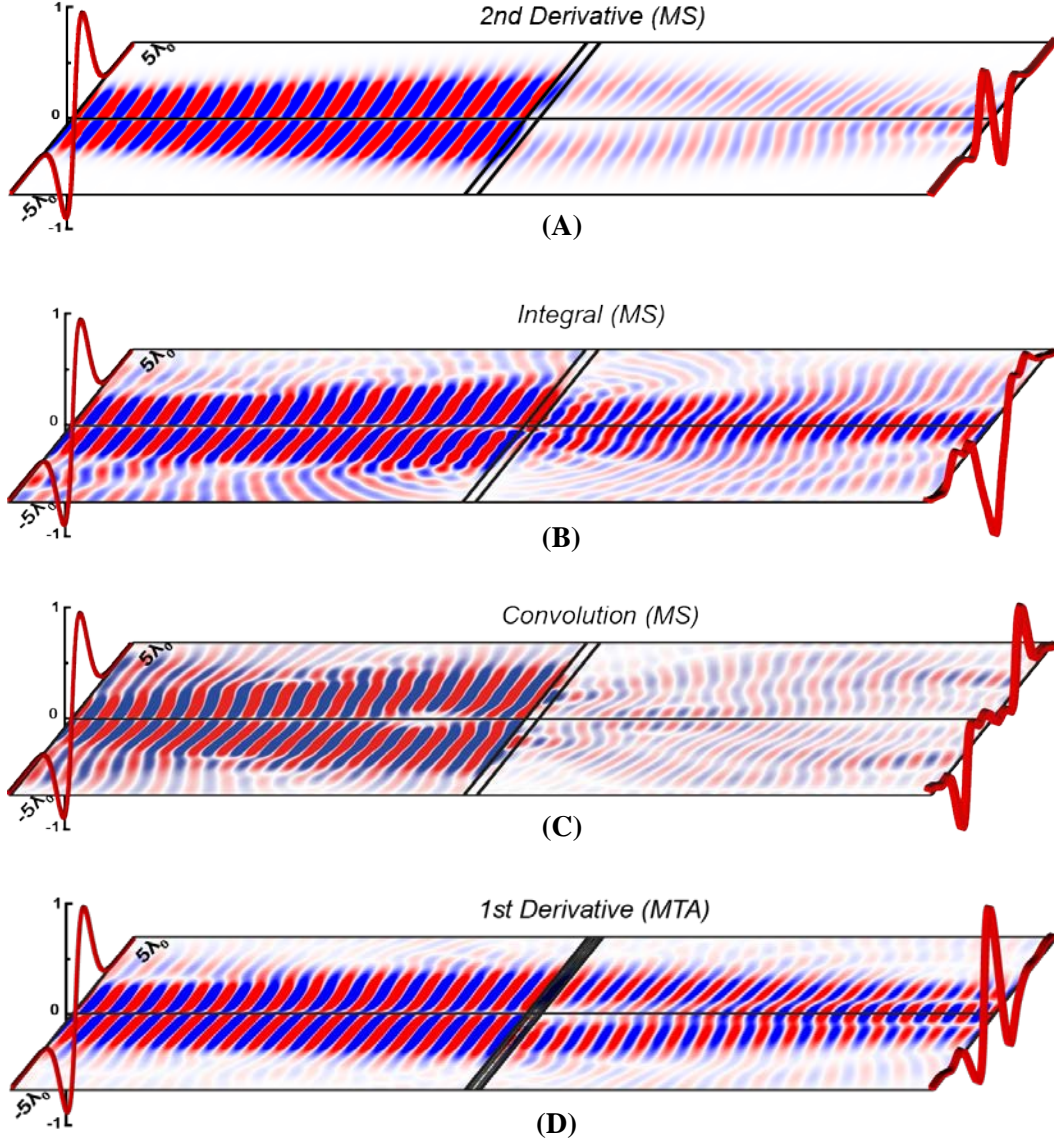
In Fig. S23B, we apply the same input function to the 5-layered GF slab that performs the convolution with a one-wavelength rectangular spatial kernel. The field profile at the output plane is compared with the expected analytical result, further confirming that the designed GF slab performs with accuracy the convolution operation.

Employing structures with symmetry breaking properties (e.g., magneto-optical materials) may realize GFS capable of producing more arbitrary GFs with broken symmetry, such as 1<sup>st</sup> differentiation. This will be the subject of future studies.



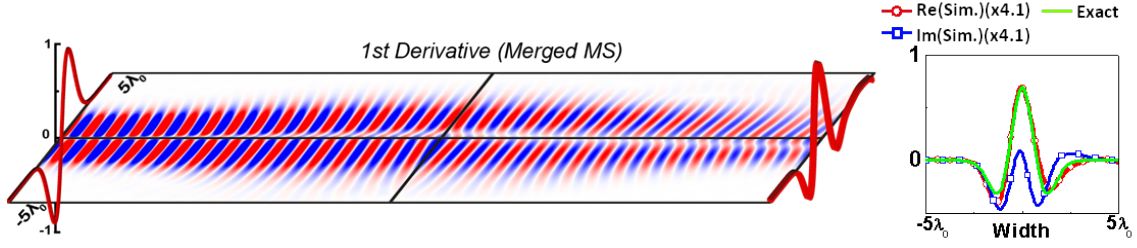
**Fig. S1**

Basic model built in COMSOL<sup>TM</sup> for the computational metamaterial system composed by GRIN(+), MS, and GRIN(+) or GRIN(-). When the MTA is used, it is inserted in the region of MS, while the rest of the system stays the same.



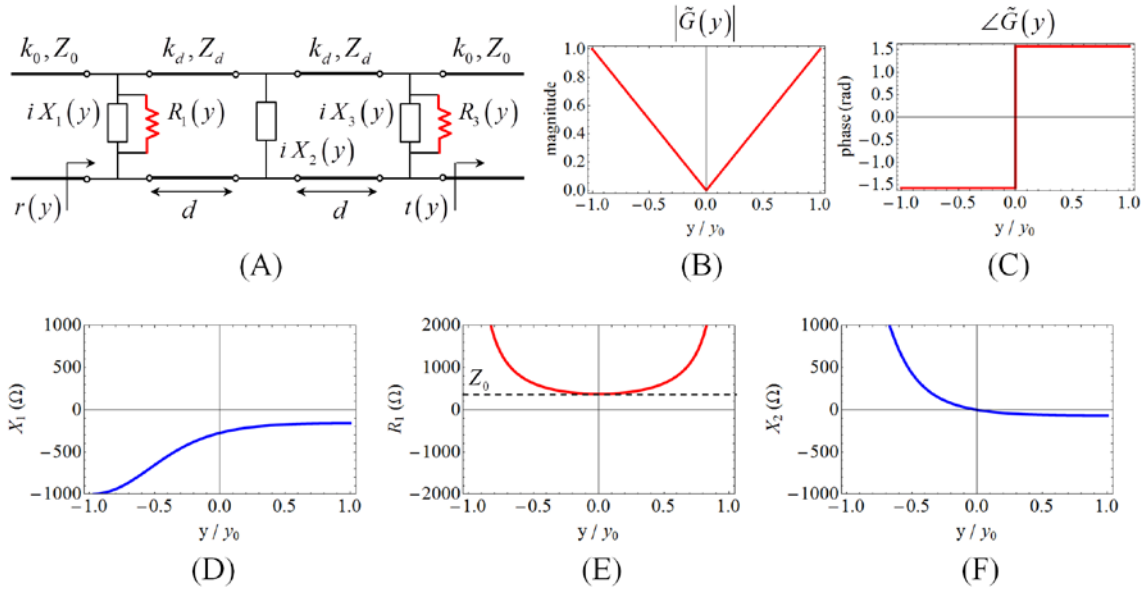
**Fig. S2**

Snapshots of z-component of electric field distribution along the system GRIN(+)/MS/GRIN(-) and GRIN(+)/MTA/GRIN(+) for different mathematical operator metastructure screens. MS and MTA have thickness  $\Delta = \lambda_o / 3$  and width  $W \cong 10\lambda_o$ . The input function  $f(y) = aye^{-y^2/b}$  is depicted in perspective on the left side of each panel as well as the obtained output functions on the right side. (A) 2<sup>nd</sup> differentiation, (B) integral, and (C) convolution operators for MS, respectively. (D) 1<sup>st</sup> differentiation for MTA, in this case both GRIN sections are conventional GRIN(+).

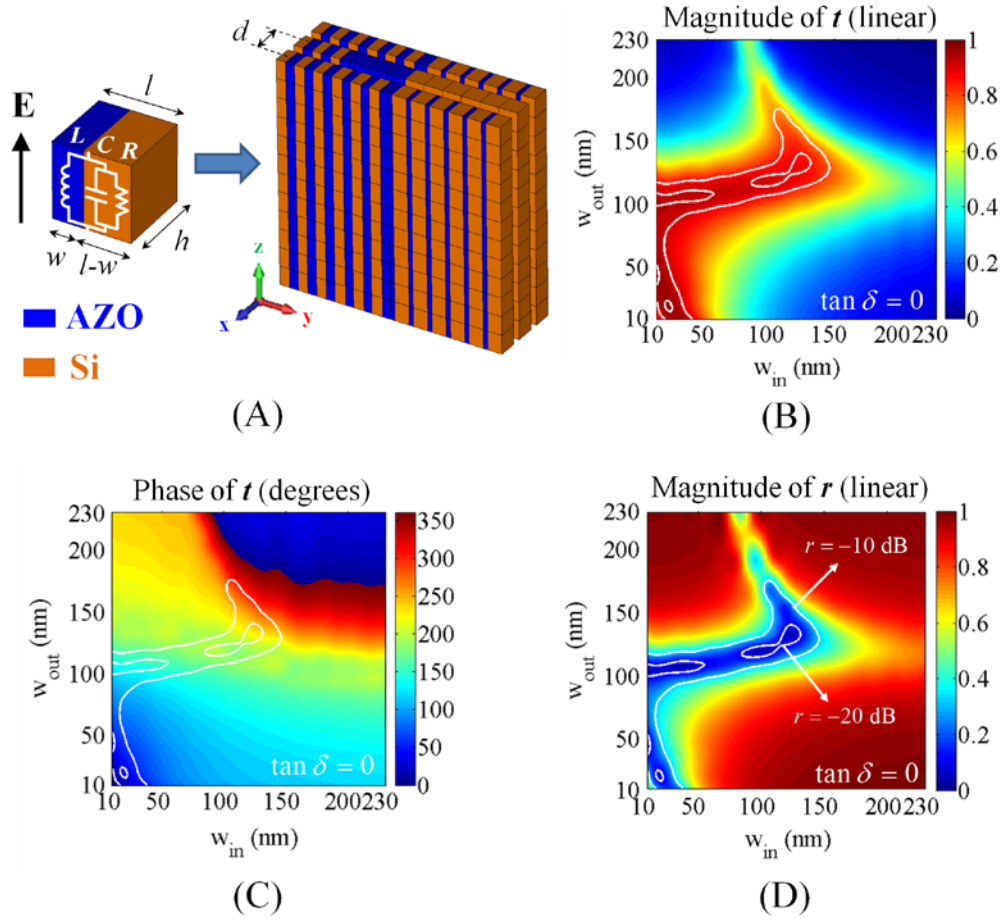


**Fig. S3**

Simulated results when the ideal MS for the 1<sup>st</sup> derivative operation is “merged” on the left of the central line with GRIN(+), and on the right of the central line, with GRIN(-), to form a single metamaterial block of length  $2L_g + \Delta$ . Panel on the left: snapshot of the  $z$ -component of the electric field distribution along the merged MS GRIN for the input function  $f(y) = aye^{-y^2/b}$ , depicted in perspective on the left side of the panel. Panel on the right: comparison among the real (red line) and imaginary (blue line) parts of the output result, obtained at  $2L_g + \Delta$ , with the analytical result (green line). No phase adjustment is used and, to facilitate the comparison, fields are multiplied by the constant factor indicated in the panel.

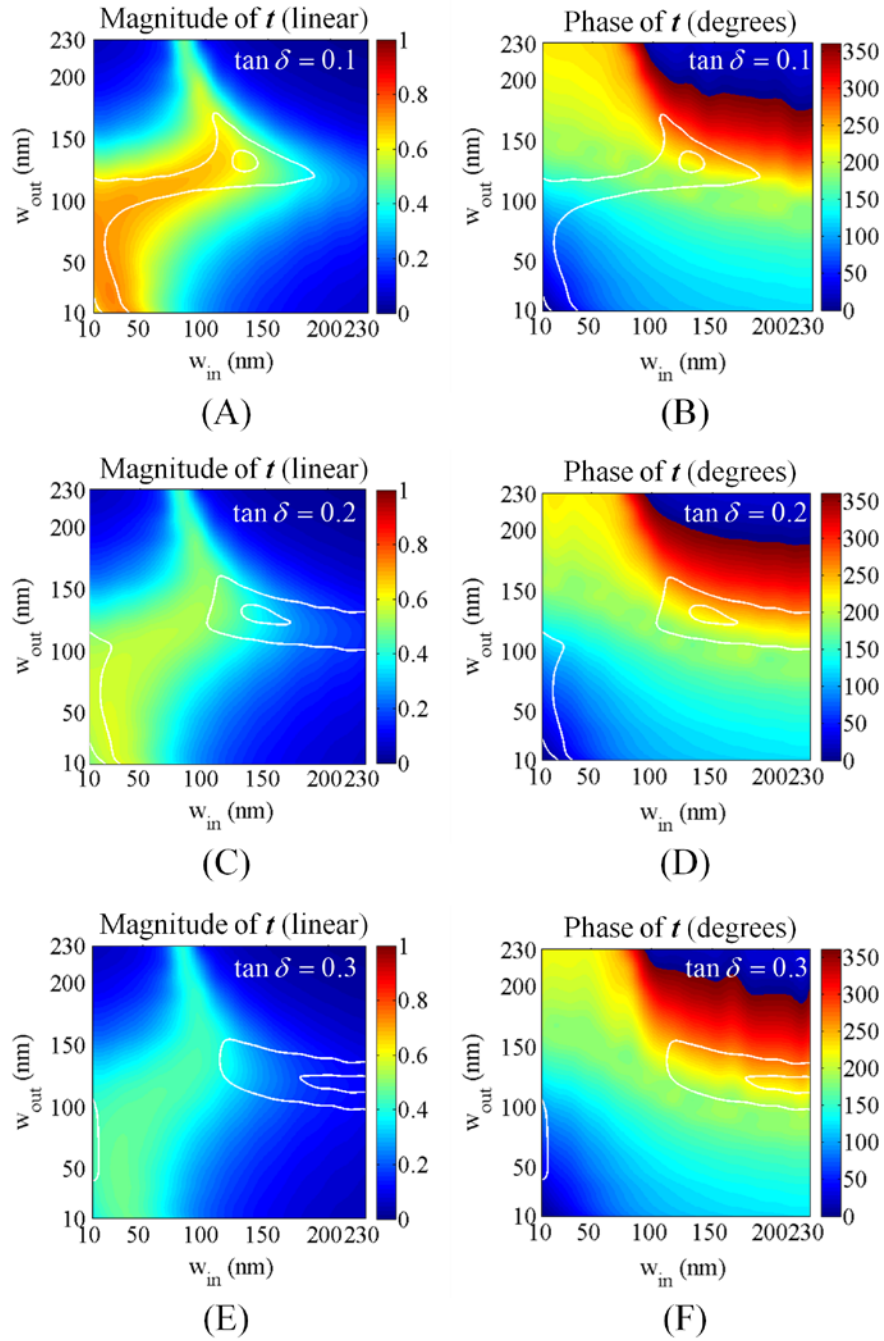
**Fig. S4**

(A) Local transmission line model of a lossy MTA composed of three parallel MSs. Arrows associated with  $r(y)$  and  $t(y)$  indicate, respectively, where the reflection and transmission coefficients are calculated. (B) Magnitude and (C) phase of the desired transfer function in the Fourier domain  $\tilde{G}(y) = iy/y_0$ . (D) Analytically calculated reactance and (E) resistance profiles of the outer MSs, and (F) reactance profile of the inner MS along the transversal direction  $y$ , which implement the desired transmission coefficient. A thin air separation of thickness  $d = \lambda_0/10$  between the MSs is assumed in this example.



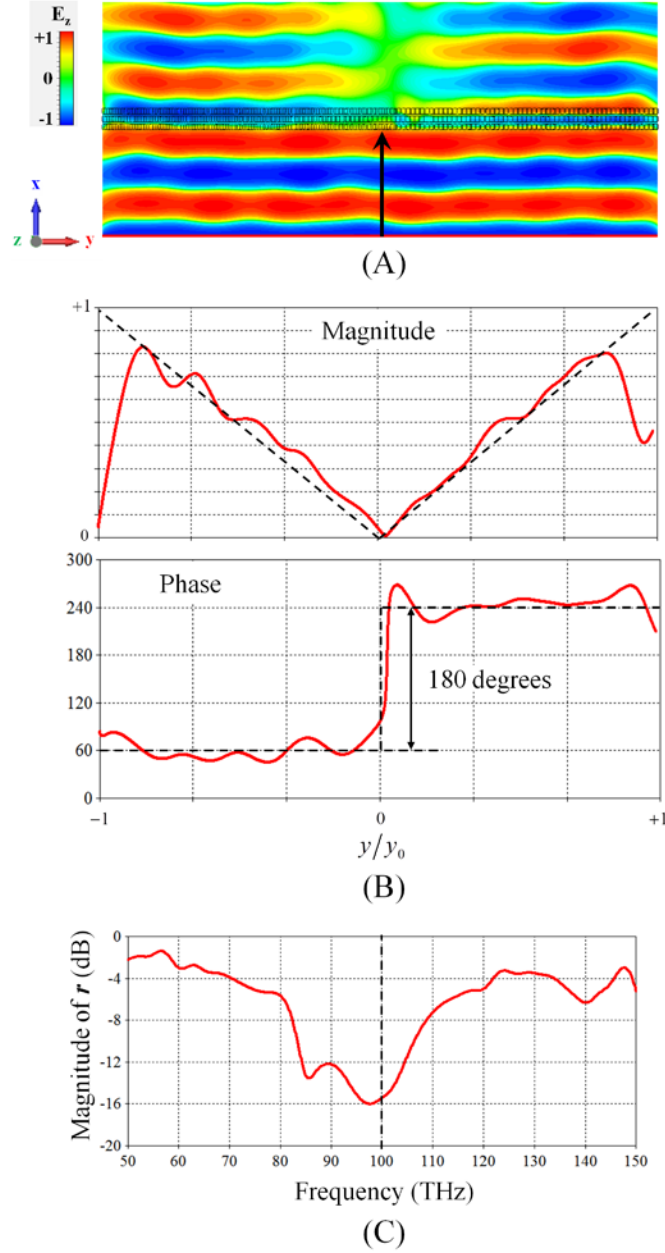
**Fig. S5**

(A) Basic building block of the MSs (left), which realizes a parallel connection between an effective inductance (plasmonic portion made of AZO) and an effective lossy capacitance (dielectric portion made of Si), for an incident electric field parallel to the  $z$  direction. Length and thickness of the unit cell are  $l = 250$  nm and  $h = 250$  nm, respectively. (right) MTA composed of a symmetric stack of three MSs with center-to-center distance  $d = \lambda_0/8$ . (B) Numerically calculated magnitude and (C) phase of the transmission coefficient  $t$  of a periodic MTA varying the width of the plasmonic portion in the internal and external MSs. (D) Magnitude of the reflection coefficient  $r$ . In all panels, the white contour lines enclose the regions of low reflection (inner contour lines correspond to  $-20$  dB, and outer to  $-10$  dB). Here, we have assumed  $\tan \delta = 0$ , i.e., lossless dielectric material.



**Fig. S6**

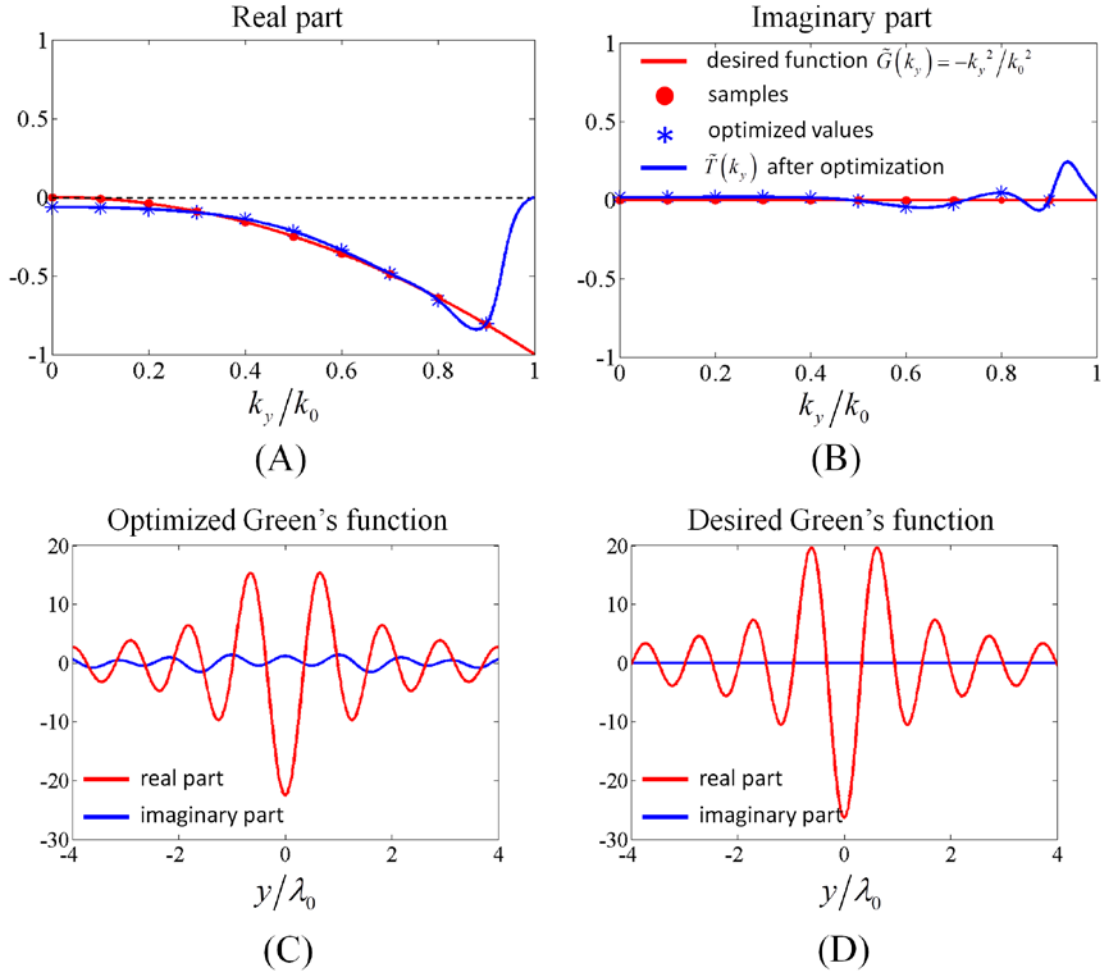
Transmission magnitude and phase of a periodic MTA, for different level of losses in the dielectric material: (A), (B)  $\tan \delta = 0.1$  ; (C), (D)  $\tan \delta = 0.2$  ; (E), (F)  $\tan \delta = 0.3$  . Notice that by increasing the loss tangent the transmission magnitude is reduced, but relatively wide low-reflection regions are preserved, as indicated by the white contour lines.



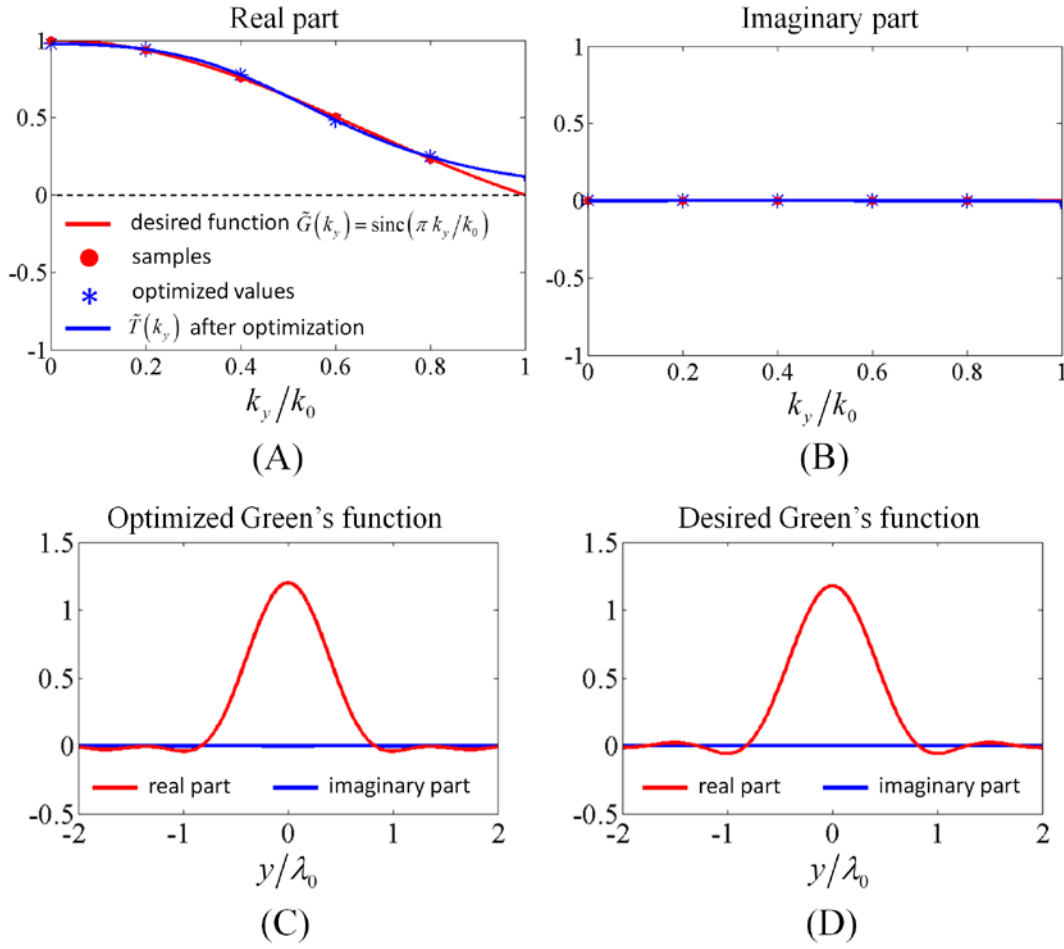
**Fig. S7**

(A) Electric field distribution (snapshot in time) for a plane wave normally incident on the designed MTA. (B) Magnitude and phase of the transmitted wave obtained right behind the structure, along the transverse direction  $y$ . Dashed lines indicate the ideal response of the desired transfer function  $\tilde{G}(y) = iy/y_0$ . Very good agreement is obtained, except understandably at the edges of the considered range since the simulated structure has finite length in the  $y$  direction. (C) Magnitude of the reflection coefficient (in dB) for normal incidence as a function of frequency, showing low reflection within a reasonable bandwidth around the central frequency.



**Fig. S8**

(A) Real and (B) imaginary parts of the optimized transmission spectrum  $\tilde{T}(k_y)$  of a 10-layer slab (blue lines), compared with the desired transformed kernel  $\tilde{G}(k_y) = -k_y^2/k_0^2$  (red lines). Red circles indicate the considered samples and the corresponding blue asterisks represent the optimized value of the transmission coefficient. (C) Green's function  $G(y)$  of the slab obtained by inverse-Fourier transforming the optimized transfer function in panels (A) and (B). (D) Desired Green's function  $G(y) = \delta''(y)$ , low-pass filtered in the propagating part of the spatial spectrum.

**Fig. S9**

(A) Real and (B) imaginary parts of the optimized transmission spectrum  $\tilde{T}(k_y)$  of a 5-layer slab (blue lines), compared with the desired transformed kernel  $\tilde{G}(k_y) = \text{sinc}(\pi k_y/k_0)$  (red lines). Red circles indicate the considered samples and the corresponding blue asterisks represent the optimized value of the transmission coefficient. (C) Green's function  $G(y)$  of the slab obtained by inverse-Fourier transforming the optimized transfer function in panels (A) and (B). (D) Desired Green's function  $G(y) = \text{rect}(y/\lambda_0)$ , low-pass filtered in the propagating part of the spatial spectrum.

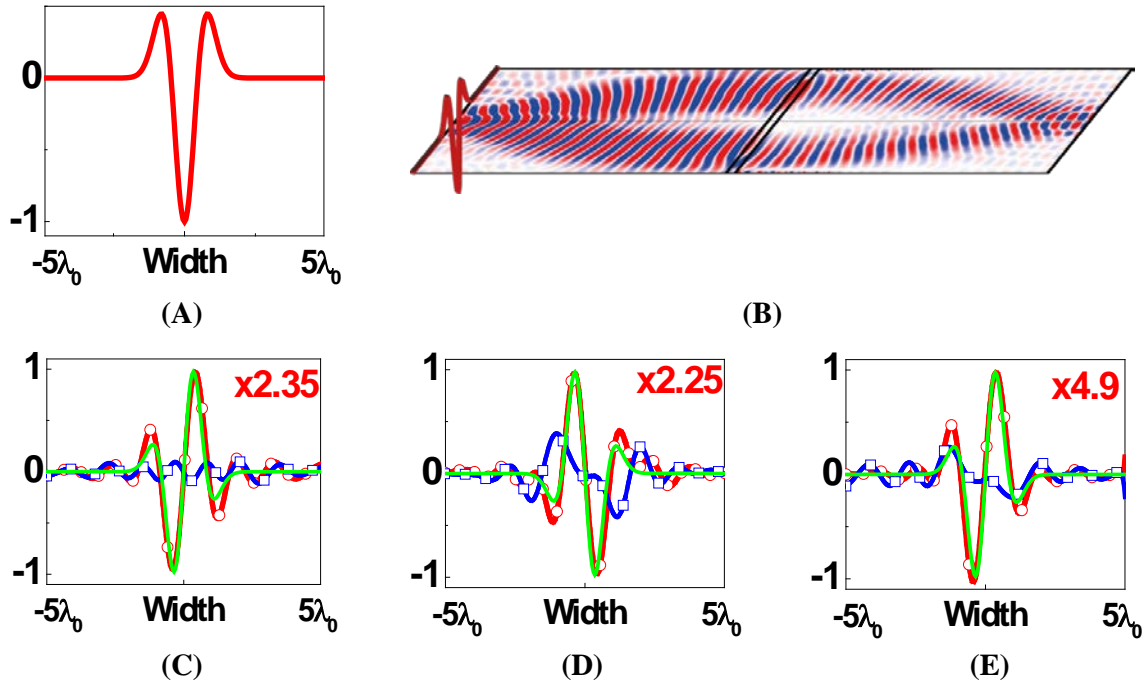


**Fig. S10**

Simulated results for the system GRIN/(MS or MTA)/GRIN that operates the 1<sup>st</sup> spatial derivative. (A) Input function  $f(y) = ce^{-y^2/d^2}(4y^2/d^2 - 2)$ . (B) Snapshot of the  $z$ -component of the electric field distribution along the GRIN with a MS of thickness  $\Delta = \lambda_0/3$  at the center. Other panels show the real (red line) and imaginary (blue line) parts of the output result, obtained at  $2L_g + \Delta$ , compared with the analytical result (green line) for the different metamaterial systems: (C) MS, (D) MTA, and (E) Merged MS. To facilitate the comparison, fields are multiplied by the constant factor indicated in each panel.

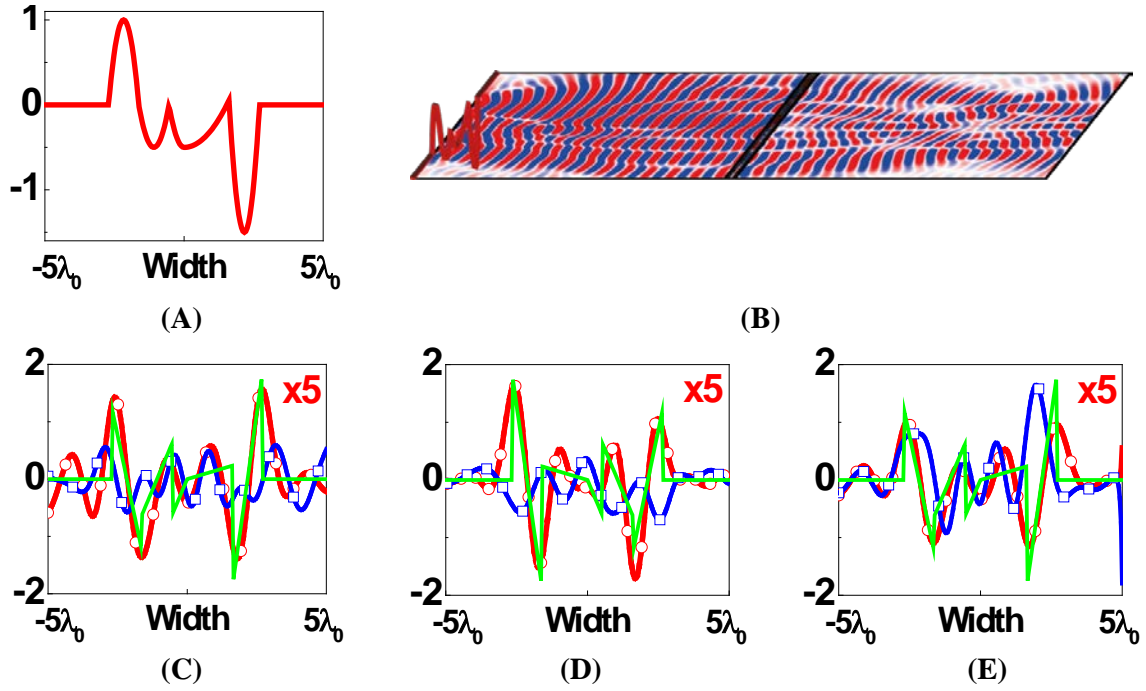


**Fig. S11**

Simulated results for the system GRIN/(MS or MTA)/GRIN that operates the 1<sup>st</sup> spatial derivative. (A) Input function: a set of quadratic polynomial functions. (B) Snapshot of the  $z$ -component of the electric field distribution along the GRIN with an MTA of thickness  $\Delta = \lambda_0/3$  at the center. Other panels show the real (red line) and imaginary (blue line) parts of the output result, obtained at  $2L_g + \Delta$  ( $L_{g\_eff}$  in the MTA case), compared with the analytical result (green line) for the different metamaterial systems: (C) MS, (D) MTA, and (E) Merged MS. To facilitate the comparison, fields are multiplied by the constant factor indicated in each panel.

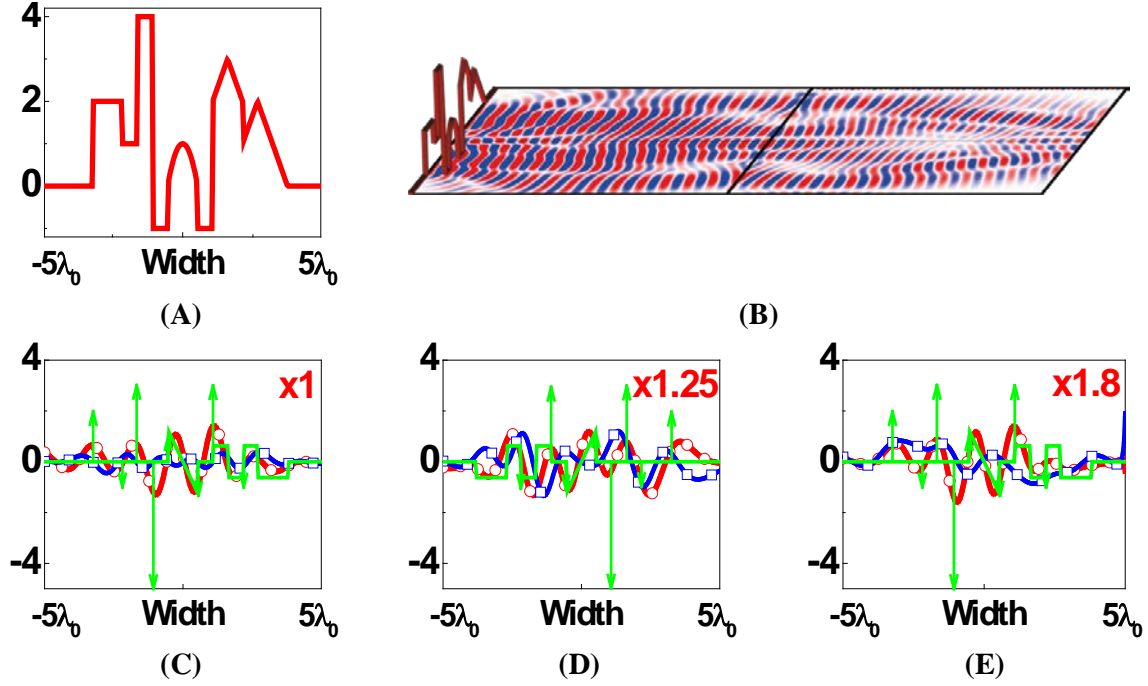


**Fig. S12**

Simulated results for the system GRIN/(MS or MTA)/GRIN that operates the 1<sup>st</sup> spatial derivative. (A) Input function: skyline. (B) Snapshot of the  $z$ - component of the electric field distribution along the GRIN with the MS material merged with GRIN (+) and GRIN(-) materials (details in the main text). Other panels show the real (red line) and imaginary (blue line) parts of the output result, obtained at  $2L_g + \Delta$  ( $L_{g\_eff}$  in the MTA case), compared with the analytical result (green line) for the different metamaterial systems: (C) MS, (D) MTA, and (E) Merged MS. To facilitate the comparison, fields are multiplied by the constant factor indicated in each panel.

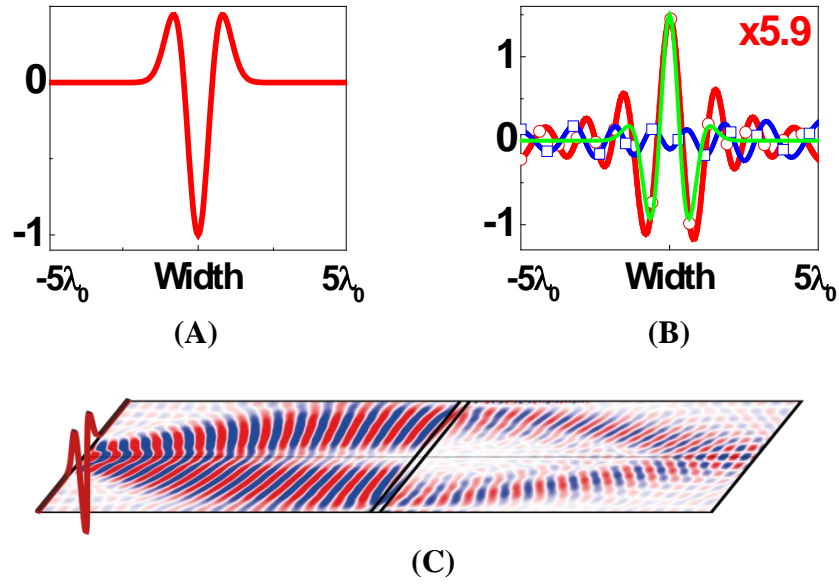


**Fig. S13**

Simulated results for the system GRIN/MS/GRIN that operates the 2<sup>nd</sup> spatial derivative. (A) Input function  $f(y) = ce^{-y^2/d^2}(4y^2/d^2 - 2)$ . (B) Output real (red line) and imaginary (blue line) parts, obtained at  $2L_g + \Delta$ , compared with the analytical result (green line). To facilitate the comparison, fields are multiplied by the constant factor indicated in the panel. (C) Snapshot of the  $z$ -component of the electric field distribution along the GRIN with a MS of thickness  $\Delta = \lambda_0/3$  at the center.

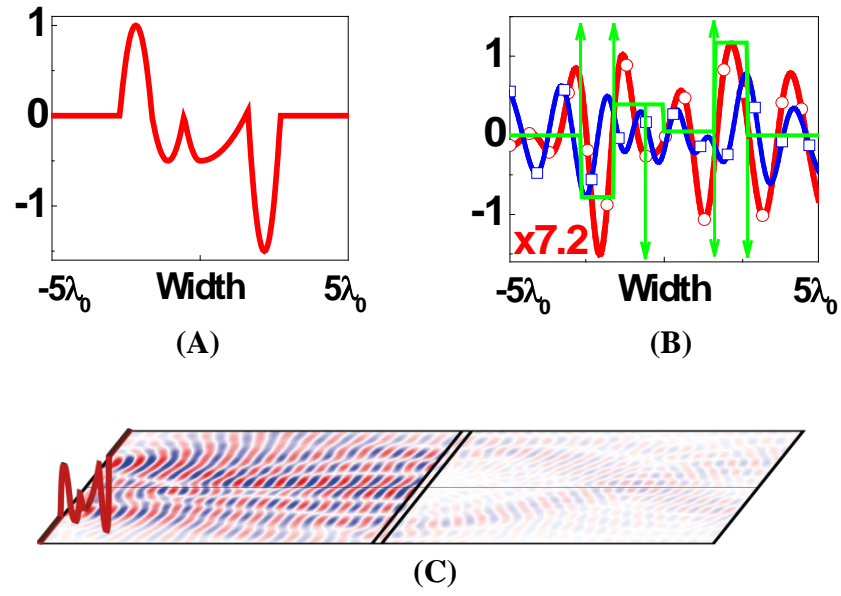


**Fig. S14**

Simulated results for the system GRIN/MS/GRIN that operates the 2<sup>nd</sup> spatial derivative. (A) Input function: set of quadratic polynomial functions. (B) Output real (red line) and imaginary (blue line) parts obtained at  $2L_g + \Delta$  compared with the analytical result (green line). To facilitate the comparison, fields are multiplied by the constant factor indicated in the panel. (C) Snapshot of the  $z$ -component of the electric field distribution along the GRIN with a MS of thickness  $\Delta = \lambda_0 / 3$  at the center.

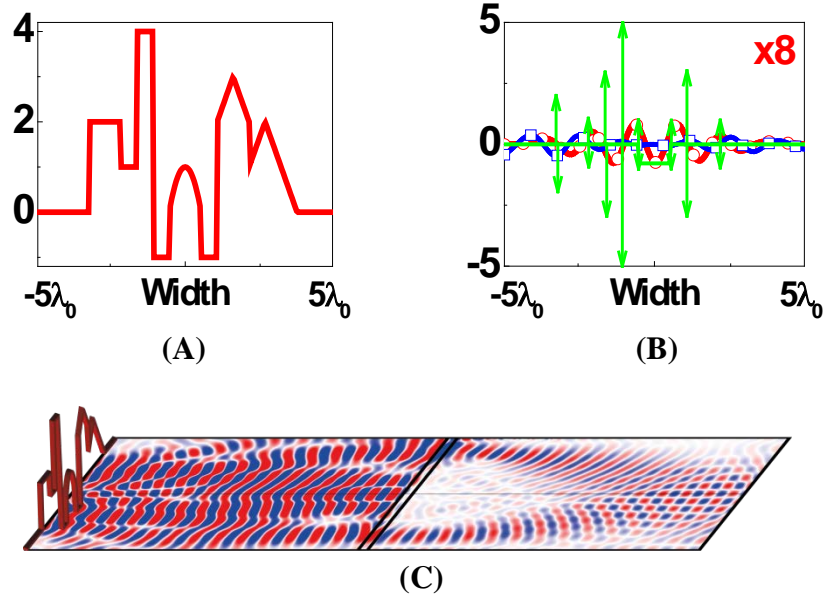


**Fig. S15**

Simulated results for the system GRIN/MS/GRIN that operates the 2<sup>nd</sup> spatial derivative. (A) Input function: skyline. (B) Output real (red line) and imaginary (blue line) parts obtained at  $2L_g + \Delta$  compared with the analytical result (green line). To facilitate the comparison, fields are multiplied by the constant factor indicated in the panel. (C) Snapshot of the  $z$ -component of the electric field distribution along the GRIN with a MS of thickness  $\Delta = \lambda_0 / 3$  at the center.



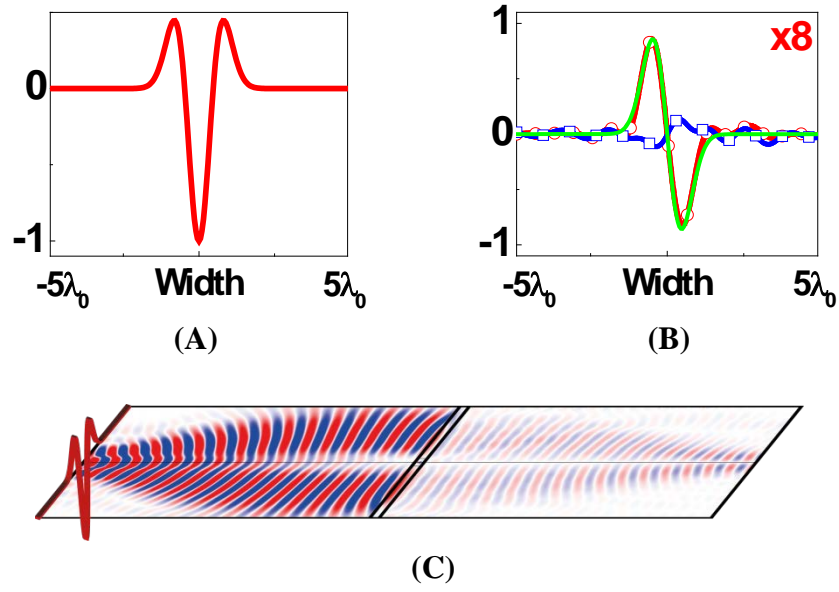


**Fig. S16**

Simulated results for the system GRIN/MS/GRIN that operates the spatial integral. (A) Input function  $f(y) = ce^{-y^2/d^2}(4y^2/d^2 - 2)$ . (B) Output real (red line) and imaginary (blue line) parts, obtained at  $2L_g + \Delta$ , compared with the analytical result (green line). To facilitate the comparison, fields are multiplied by the constant factor indicated in the panel. (C) Snapshot of z-component of the electric field distribution along the GRIN with a MS of thickness  $\Delta = \lambda_0 / 3$  at the center.

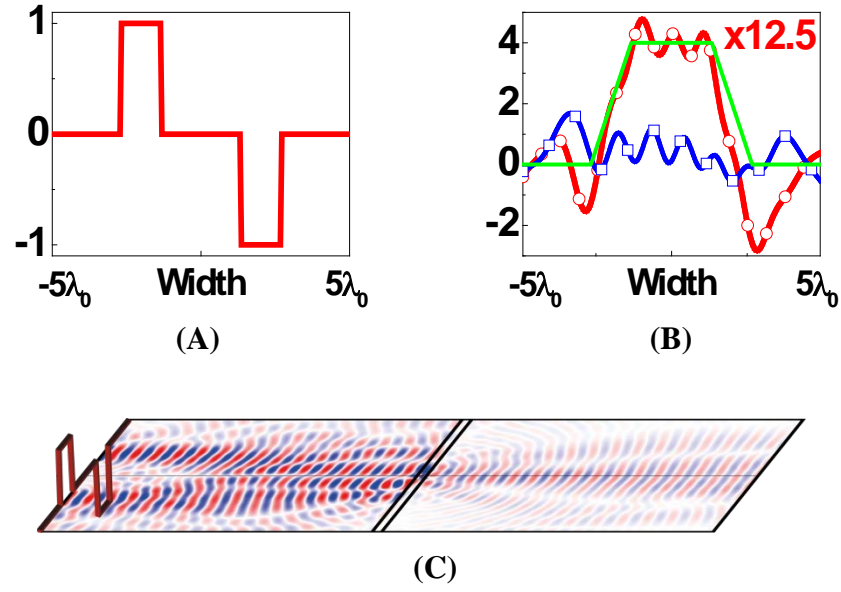


**Fig. S17**

Simulated results for the system GRIN/MS/GRIN that operates the spatial integral. (A) Input function: two inverted rectangular functions. (B) Output real (red line) and imaginary (blue line) parts, obtained at  $2L_g + \Delta$ , compared with the analytical result (green line). To facilitate the comparison, fields are multiplied by the constant factor indicated in the panel. (C) Snapshot of the  $z$ -component of the electric field distribution along the GRIN with a MS of  $\Delta = \lambda_0 / 3$  at the center.

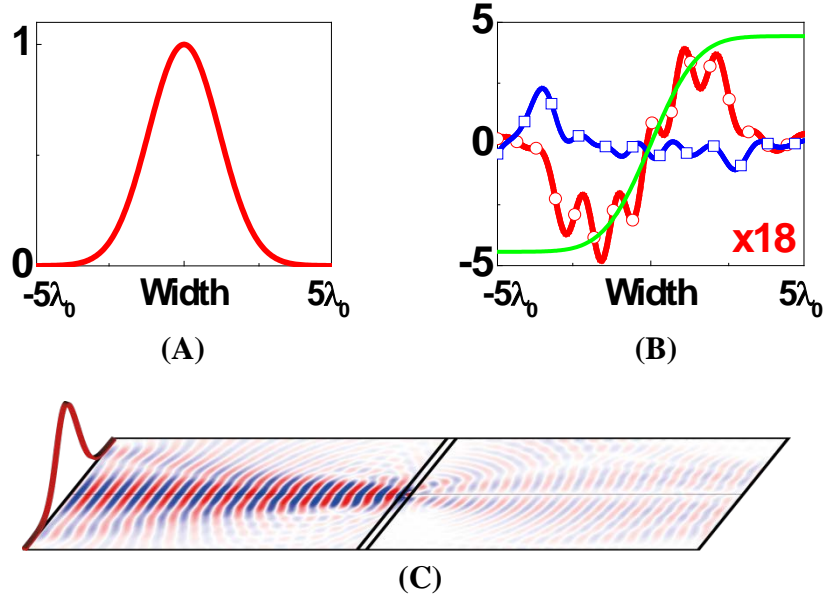


**Fig. S18**

Simulated results for the system GRIN/MS/GRIN that operates the spatial integral. (A) Input function  $f(y) = e^{-y^2/m^2}$ . (B) Output real (red line) and imaginary (blue line) parts, obtained at  $2L_g + \Delta$ , compared with the analytical result (green line). To facilitate the comparison, fields are multiplied by the constant factor indicated in the panel. (C) Snapshot of the  $z$ -component of the electric field distribution along the GRIN with a MS of  $\Delta = \lambda_0 / 3$  at the center.

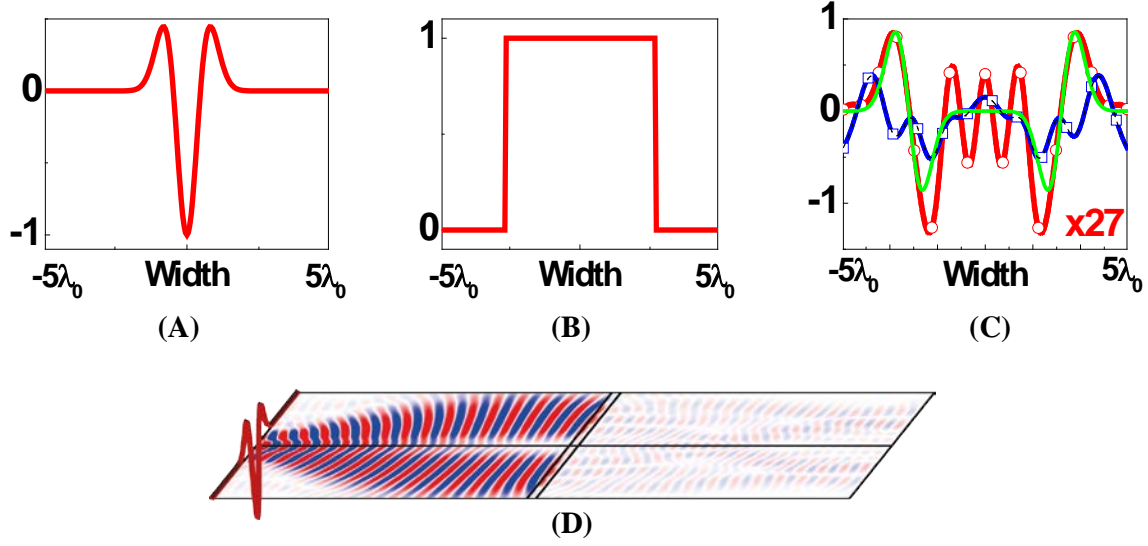


**Fig. S19**

Simulated results for the system GRIN/MS/GRIN that operates the spatial convolution. (A) Input function:  $f(y) = ce^{-y^2/d^2}(4y^2/d^2 - 2)$ . (B) Kernel: rectangular function with width of  $5.33\lambda_0$ . (C) Output real (red line) and imaginary (blue line) parts, obtained at  $2L_g + \Delta$ , compared with the analytical result (green line). To facilitate the comparison, fields are multiplied by the constant factor indicated in the panel. (D) Snapshot of the  $z$ -component of the electric field distribution along the GRIN with a MS of thickness  $\Delta = \lambda_0 / 3$  at the center.

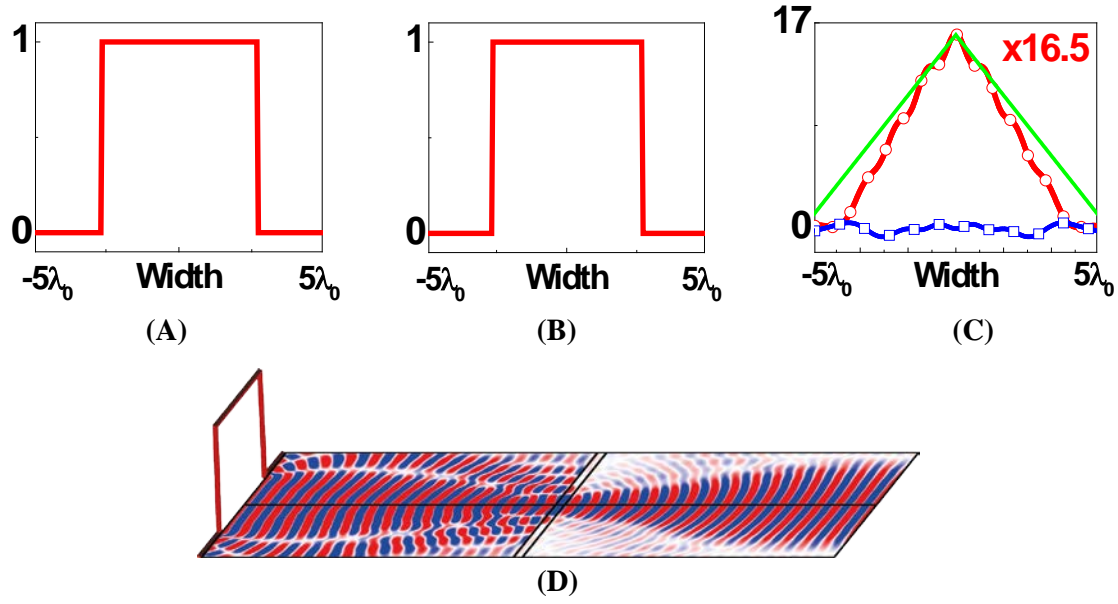


**Fig. S20**

Simulated results for the system GRIN/MS/GRIN that operates the spatial convolution. (A) Input function: rectangular function with width of  $5.33\lambda_0$ . (B) Kernel: rectangular function with width of  $5.33\lambda_0$ . (C) Output real (red line) and imaginary (blue line) parts, obtained at  $2L_g + \Delta$ , compared with the analytical result (green line). To facilitate the comparison, fields are multiplied by the constant factor indicated in the panel. (D) Snapshot of the  $z$ -component of the electric field distribution along the GRIN with a MS of thickness  $\Delta = \lambda_0 / 3$  at the center.

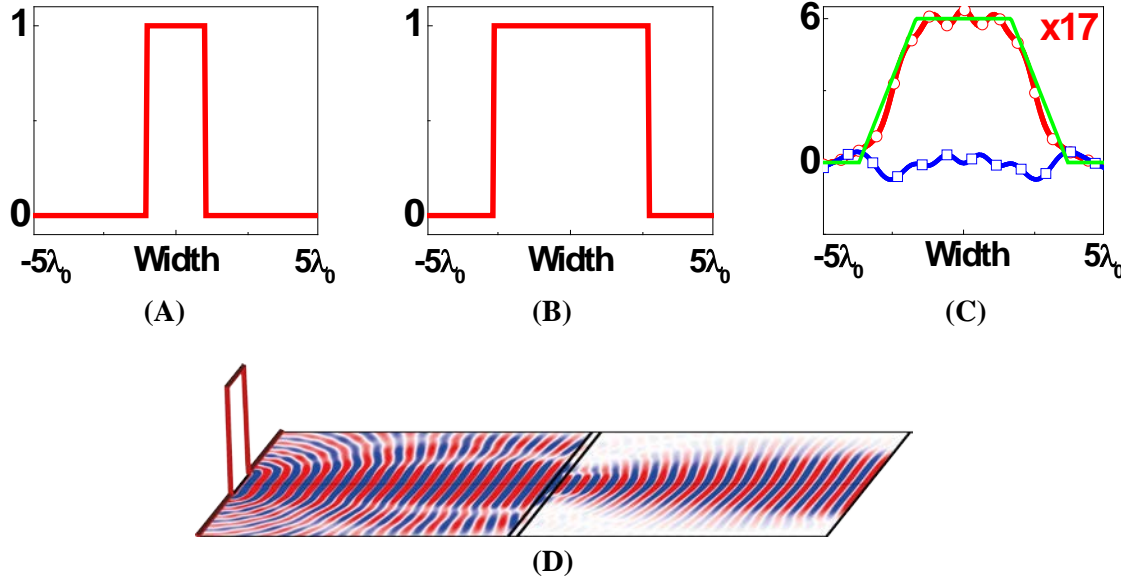


**Fig. S21**

Simulated results for the system GRIN/MS/GRIN that operates the spatial convolution. (A) Input function: rectangular function with width of  $2\lambda_0$ . (B) Kernel: rectangular function with width of  $5.33\lambda_0$ . (C) Output real (red line) and imaginary (blue line) parts, obtained at  $2L_g + \Delta$ , compared with the analytical result (green line). To facilitate the comparison, fields are multiplied by the constant factor indicated in the panel. (D) Snapshot of the  $z$ -component of the electric field distribution along the GRIN with a MS of thickness  $\Delta = \lambda_0 / 3$  at the center.

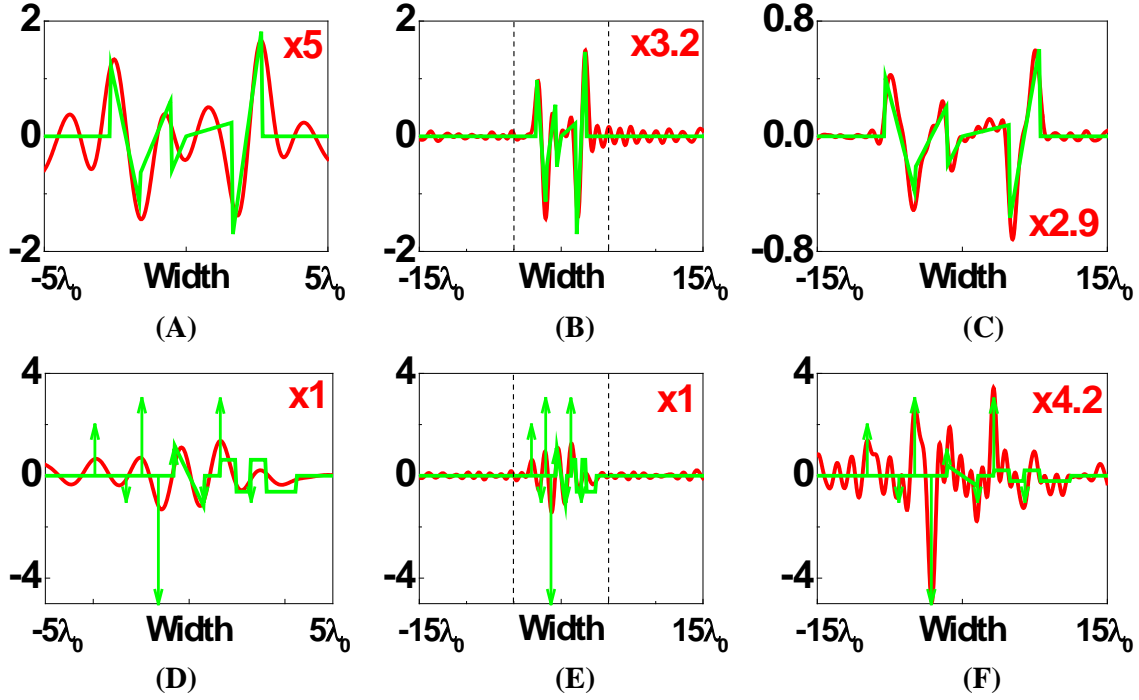


**Fig. S22**

Real part of output simulated profiles (red lines) observed at  $2L_g + \Delta$  for the system GRIN(+)/MS/GRIN(-) that operates the 1<sup>st</sup> spatial derivative for scaled GRIN waveguides, compared with analytical results (green lines) for scaled GRIN and input functions. For the following cases, input function is the set of quadratic polynomial functions presented in Fig. S4A: (A) Non-scaled input function (same width as in Fig. S4A), and  $W = 10\lambda_0$ ; (B) Non-scaled input function and  $W = 30\lambda_0$ ; and (C) Input function width scaled up by three times and  $W = 30\lambda_0$ . For the other panels, input function is the Austin skyline borders presented in Fig. S5A: (D) Non-scaled input function (same width as in Fig. S5A), and  $W = 10\lambda_0$ ; (E) Non-scaled input function and  $W = 30\lambda_0$ ; (F) Input function width scaled up by three times and  $W = 30\lambda_0$ . To facilitate the comparison, fields are multiplied by the constant factor indicated in each panel.

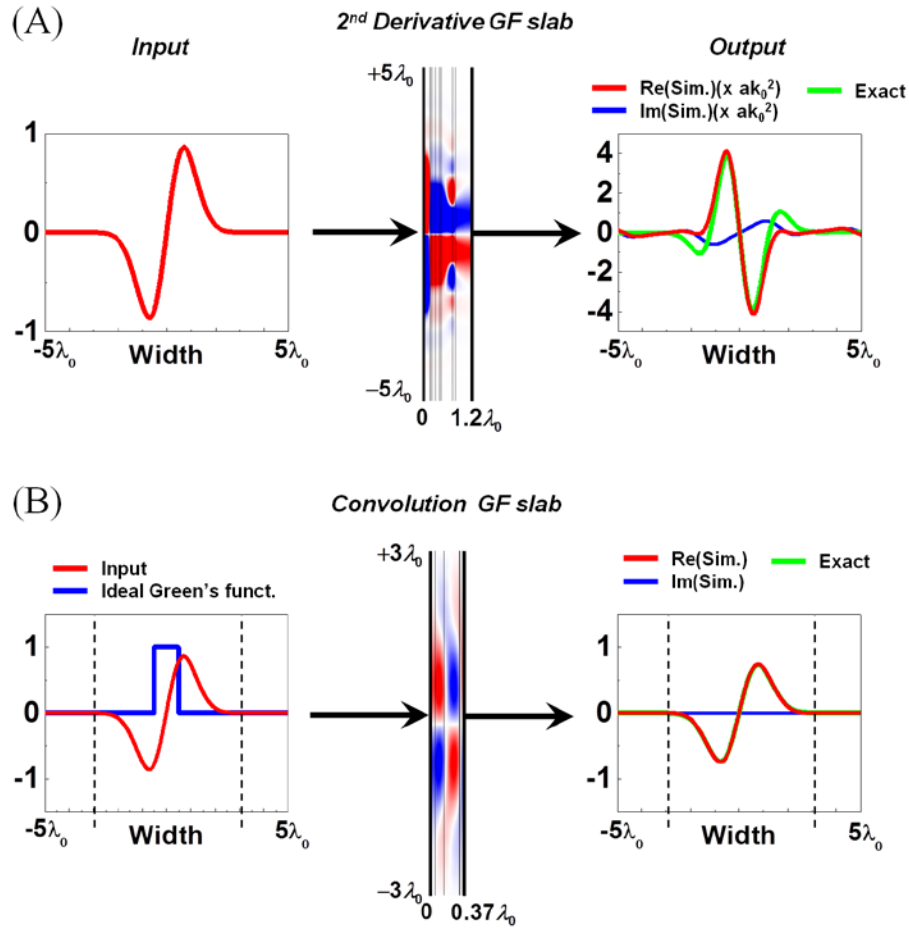


**Fig. S23**

(A) GF slab designed to perform 2<sup>nd</sup> spatial differentiation, composed of 10 layers and a total thickness  $L \approx 1.2\lambda_0$  (design parameters provided in the Materials and Methods section). Simulated wave propagation ( $z$ -component of the magnetic field) throughout the slab for an input function  $f(y) = ay e^{-y^2/b}$  (left panel). As in Fig. 3 of the main text, the right panel shows the comparison between simulated output (real part: red, imaginary part: blue) and the analytical (green) results. (B) 5-layered GF slab, with total thickness  $L = 0.37\lambda_0$  (details in the Materials and Methods section), designed to perform the convolution with a rectangular Green's function kernel of width  $\lambda_0$ , shown in blue in the left panel. The results for the same input function as in (A) are presented in the right panel. The field distribution in (B) is shown in a limited lateral region for clarity, indicated by the dashed lines.



	1	2	3	4	5	6	7	8	9	10
$\varepsilon_r$	13.85	5.98	4.44	0.06	0.03	0.01	-0.003	-2.12	2.30	0.08
$d$	$\frac{\lambda_0}{293.4}$	$\frac{\lambda_0}{6.0}$	$\frac{\lambda_0}{212.9}$	$\frac{\lambda_0}{24.2}$	$\frac{\lambda_0}{12.1}$	$\frac{\lambda_0}{9.8}$	$\frac{\lambda_0}{25.0}$	$\frac{\lambda_0}{3.6}$	$\frac{\lambda_0}{14.5}$	$\frac{\lambda_0}{2.4}$

**Table S1.**

Relative permittivity and thickness of each layer, for the case of 2<sup>nd</sup> differentiation operator, calculated with our fast synthesis approach based on the simplex optimization method.

	1	2	3	4	5
$\varepsilon_r$	-0.08	9.88	7.86	0.11	13.68
$d$	$\frac{\lambda_0}{21.2}$	$\frac{\lambda_0}{9.7}$	$\frac{\lambda_0}{5.4}$	$\frac{\lambda_0}{174.1}$	$\frac{\lambda_0}{30.7}$

**Table S2.**

Relative permittivity and thickness of each layer for the case of convolution operator, calculated with our fast synthesis approach based on the simplex optimization method. The resulting multi-layered slab implements the desired rectangular kernel function.

## References

1. N. Engheta, R. W. Ziolkowski, Eds., *Metamaterials—Physics and Engineering Explorations* (IEEE-Wiley, New York, 2006).
2. G. V. Eleftheriades, K. G. Balmain, *Negative-Refractive Metamaterials* (IEEE, New York, 2005).
3. D. R. Smith, J. B. Pendry, M. C. K. Wiltshire, Metamaterials and negative refractive index. *Science* **305**, 788–792 (2004). [doi:10.1126/science.1096796](https://doi.org/10.1126/science.1096796) [Medline](#)
4. C. Caloz, T. Itoh, *Electromagnetic Metamaterials—Transmission Line Theory and Microwave Applications* (IEEE-Wiley, New York, 2006).
5. W. Cai, V. Shalaev, *Optical Metamaterials: Fundamentals and Applications* (Springer, New York, 2010).
6. J. B. Pendry, D. Schurig, D. R. Smith, Controlling electromagnetic fields. *Science* **312**, 1780–1782 (2006). [doi:10.1126/science.1125907](https://doi.org/10.1126/science.1125907) [Medline](#)
7. U. Leonhardt, Optical conformal mapping. *Science* **312**, 1777–1780 (2006). [doi:10.1126/science.1126493](https://doi.org/10.1126/science.1126493) [Medline](#)
8. A. Alù, N. Engheta, Achieving transparency with plasmonic and metamaterial coatings. *Phys. Rev. E* **72**, 016623 (2005). [doi:10.1103/PhysRevE.72.016623](https://doi.org/10.1103/PhysRevE.72.016623) [Medline](#)
9. A. Vakil, N. Engheta, Transformation optics using graphene. *Science* **332**, 1291–1294 (2011). [doi:10.1126/science.1202691](https://doi.org/10.1126/science.1202691) [Medline](#)
10. E. F. Kuester, M. A. Mohamed, M. Piket-May, C. L. Holloway, Averaged transition conditions for electromagnetic fields at a metafilm. *IEEE Trans. Antenn. Propag.* **51**, 2641–2651 (2003). [doi:10.1109/TAP.2003.817560](https://doi.org/10.1109/TAP.2003.817560)
11. N. Yu, P. Genevet, M. A. Kats, F. Aieta, J.-P. Tetienne, F. Capasso, Z. Gaburro, Light propagation with phase discontinuities: Generalized laws of reflection and refraction. *Science* **334**, 333–337 (2011). [doi:10.1126/science.1210713](https://doi.org/10.1126/science.1210713) [Medline](#)

12. X. Ni, N. K. Emani, A. V. Kildishev, A. Boltasseva, V. M. Shalaev, Broadband light bending with plasmonic nanoantennas. *Science* **335**, 427 (2012). [doi:10.1126/science.1214686](https://doi.org/10.1126/science.1214686)  
[Medline](#)
13. Y. Zhao, M. A. Belkin, A. Alù, Twisted optical metamaterials for planarized ultrathin broadband circular polarizers. *Nat. Commun.* **3**, 870 (2012). [doi:10.1038/ncomms1877](https://doi.org/10.1038/ncomms1877)  
[Medline](#)
14. A. Pandey, N. M. Litchinitser, Nonlinear light concentrators. *Opt. Lett.* **37**, 5238–5240 (2012). [doi:10.1364/OL.37.005238](https://doi.org/10.1364/OL.37.005238) [Medline](#)
15. Y. Lai, J. Ng, H. Chen, D. Han, J. Xiao, Z.-Q. Zhang, C. T. Chan, Illusion optics: The optical transformation of an object into another object. *Phys. Rev. Lett.* **102**, 253902 (2009).  
[doi:10.1103/PhysRevLett.102.253902](https://doi.org/10.1103/PhysRevLett.102.253902) [Medline](#)
16. D. de Solla Price, A history of calculating machines. *IEEE Micro.* **4**, 22–52 (1984).  
[doi:10.1109/MM.1984.291305](https://doi.org/10.1109/MM.1984.291305)
17. A. B. Clymer, The mechanical analog computers of Hannibal Ford and William Newell. *IEEE Ann. Hist. Comput.* **15**, 19 (1993). [doi:10.1109/85.207741](https://doi.org/10.1109/85.207741)
18. Computer History Museum, [www.computerhistory.org/revolution/analog-computers/3](http://www.computerhistory.org/revolution/analog-computers/3).
19. G. W. Milton, Complete characterization of the macroscopic deformations of periodic unimode metamaterials of rigid bars and pivots. *J. Mech. Phys. Solids* **61**, 1543–1560 (2013). [doi:10.1016/j.jmps.2012.08.011](https://doi.org/10.1016/j.jmps.2012.08.011)
20. A. B. Kempe, On a general method of describing plane curves of the  $n$ th degree by linkwork. *Proc. London Math. Soc.* **7**, 213 (1876).
21. A. Weiner, Femtosecond pulse shaping using spatial light modulators. *Rev. Sci. Instrum.* **71**, 1929 (2000). [doi:10.1063/1.1150614](https://doi.org/10.1063/1.1150614)
22. D. Casasent, Spatial light modulators. *Proc. IEEE* **65**, 143–157 (1977).
23. J. Goodman, *Introduction to Fourier Optics* (Roberts & Co., Englewood, CO, ed. 3, 2005).
24. H. M. Ozaktas, D. Mendlovic, Fractional Fourier transforms and their optical implementation. II. *J. Opt. Soc. Am. A* **10**, 2522 (1993). [doi:10.1364/JOSAA.10.002522](https://doi.org/10.1364/JOSAA.10.002522)

25. J. B. Pendry, S. A. Ramakrishna, Focusing light using negative refraction. *J. Phys. Condens. Matter* **15**, 6345–6364 (2003). [doi:10.1088/0953-8984/15/37/004](https://doi.org/10.1088/0953-8984/15/37/004)
26. G. V. Naik, J. Kim, A. Boltasseva, Oxides and nitrides as alternative plasmonic materials in the optical range. *Opt. Mater. Express* **1**, 1090 (2011). [doi:10.1364/OME.1.001090](https://doi.org/10.1364/OME.1.001090)
27. F. Monticone, N. M. Estakhri, A. Alù, Full control of nanoscale optical transmission with a composite metascreen. *Phys. Rev. Lett.* **110**, 203903 (2013).  
[doi:10.1103/PhysRevLett.110.203903](https://doi.org/10.1103/PhysRevLett.110.203903)
28. See supplementary materials on *Science* Online.
29. G. Castaldi, V. Galdi, A. Alù, N. Engheta, Nonlocal transformation optics. *Phys. Rev. Lett.* **108**, 063902 (2012). [doi:10.1103/PhysRevLett.108.063902](https://doi.org/10.1103/PhysRevLett.108.063902) [Medline](#)
30. R. C. Gonzalez, R. E. Woods, *Digital Image Processing* (Prentice Hall, New York, 2008).
31. A. Alù, Wave-shaping surfaces. *Physics* **6**, 53 (2013). [doi:10.1103/Physics.6.53](https://doi.org/10.1103/Physics.6.53)
32. N. Engheta, A. Salandrino, A. Alù, Circuit elements at optical frequencies: Nanoinductors, nanocapacitors, and nanoresistors. *Phys. Rev. Lett.* **95**, 095504 (2005).  
[doi:10.1103/PhysRevLett.95.095504](https://doi.org/10.1103/PhysRevLett.95.095504) [Medline](#)
33. N. Engheta, Circuits with light at nanoscales: Optical nanocircuits inspired by metamaterials. *Science* **317**, 1698–1702 (2007). [doi:10.1126/science.1133268](https://doi.org/10.1126/science.1133268) [Medline](#)
34. H. W. Icenogle, B. C. Platt, W. L. Wolfe, Refractive indexes and temperature coefficients of germanium and silicon. *Appl. Opt.* **15**, 2348–2351 (1976). [doi:10.1364/AO.15.002348](https://doi.org/10.1364/AO.15.002348)  
[Medline](#)
35. J. C. Lagarias, J. A. Reeds, M. H. Wright, P. E. Wright, Convergence properties of the Nelder-Mead simplex method in low dimensions. *SIAM J. Optim.* **9**, 112–147 (1998).  
[doi:10.1137/S1052623496303470](https://doi.org/10.1137/S1052623496303470)